



Title	Energy conservation using new structured-core and transparent vacuum insulation panels: Numerical simulation with experimental validation
Author(s)	Katsura, Takao; Radwan, Ali; Yang, Zhang; Nakamura, Makoto; Nagano, Katsunori
Citation	Solar energy, 193, 885-905 https://doi.org/10.1016/j.solener.2019.09.083
Issue Date	2019-11-15
Doc URL	http://hdl.handle.net/2115/83280
Rights	© <2019>. This manuscript version is made available under the CC-BY-NC-ND 4.0 license http://creativecommons.org/licenses/by-nc-nd/4.0/
Rights(URL)	http://creativecommons.org/licenses/by-nc-nd/4.0/
Type	article (author version)
File Information	Revised manuscript2.pdf



[Instructions for use](#)

Energy Conservation using New Structured-Core and Transparent Vacuum Insulation Panels: Numerical Simulation with Experimental Validation

Takao Katsura*¹, Ali Radwan^{1,2}, Zhang Yang³, Makoto Nakamura¹, Katsunori Nagano¹

¹Division of Human Environmental Systems, Faculty of Engineering, Hokkaido University,
N13-W8, Kita-ku, Sapporo 060-8628, Japan

²Department of Mechanical Power Engineering, Mansoura University, El-Mansoura 35516, Egypt

³Country Garden, Beijiao Town, Shunde District, Foshan, Guangdong 528312, China

* Corresponding author: Tel: +81-11-706-6284, e-mail: katsura@eng.hokudai.ac.jp

Abstract

The rate of heat gain or heat loss from the windows of existing buildings represents a large portion of building energy consumption in harsh hot or cold regions, respectively. Therefore, several thermal insulation technologies have been applied in new buildings. However, these technologies are difficult to implement in existing buildings. Therefore, this study proposes a new, low-cost insulation method using slim, transparent panels with structured cores, for the windows of existing buildings. To do this, five new distinct designs of vacuum insulation panels (VIPs) are proposed to retrofit insulation for the windows of existing buildings. The VIPs comprise a hollow-frame structured-core material encapsulated in a transparent multi-layered polymeric envelope. The effective thermal conductivity of VIPs with different spacers, namely, peek, modified peek, mesh, silica aerogel, and frame, are evaluated at different pressure levels. The spacers are 3D-printed and experimentally-examined. A 3D thermal model is developed and validated using the experimental results of the present work and results from the literature. First, the influences of spacer structure and vacuum pressure on the centre-of-panel thermal conductivity, light transparency, and VIP production costs are evaluated. Second, three different trial manufacturing methods for these VIPs are proposed and compared. Finally, the annual building heat gain and heat loss in two different harsh hot and cold regions, respectively, in Japan are estimated while applying these new proposed VIP designs to the existing windows. The results indicate that VIPs with frame and mesh spacers accomplish better insulation performance, with a centre-of-panel thermal conductivity of 7×10^{-3} W/m.K at a pressure of 1 Pa. Further, the VIP with the peek spacer accomplishes the highest light transparency (0.88). Furthermore, using a frame-type VIP with a total thickness of 3 mm attached to an existing window as a curtain decreases the space heat loss by approximately 69.5%, whereas the light transparency decreases to 75 %. In that regard, using a frame-type VIP attached to 3 mm-glass windows decreases window insulation costs by 72 % compared with vacuum glazing thermal insulation.

Keywords: Vacuum insulation panel; structured-core and transparent; retrofitting insulation; surface-to-surface radiation; 3D modelling

Highlights

- Five distinct structured-core and transparent vacuum insulation panels are analysed.
- A 3D model is used to predict the insulation ability.
- VIPs with mesh and frame spacers achieve better insulation performance.

- 40 • The proposed VIPs are cost-effective when compared with silica aerogels and vacuum glazing.
- 41 • VIPs with pillar spacers provide the highest light transparency.

42 1. Introduction

43 Environmental problems and energy exhaustion have become major global issues. The annual
44 energy consumption is increasing every year, and the amount of environmental pollution is accelerating. In
45 this regard, many energy-saving technologies for building applications have been installed in new buildings.
46 Meanwhile, old buildings are often protected for their aesthetical and historical contributions to society.
47 However, the aforementioned energy-saving technologies are rarely installed in such existing buildings.
48 The insulation ability of the existing buildings is poor; therefore, it is vital to improving their insulation
49 performance. Vacuum insulation panels (VIPs) are panels characterised by very low thermal conductivity
50 as compared to traditional insulating materials (Fricke et al., 2008). For this reason, they represent a
51 promising solution for improving the thermal behaviour of buildings, especially in the case of energy
52 retrofitting (where higher performance and smaller thicknesses are desirable) (Boafo et al., 2019). Further,
53 it is essential to decrease the summer heat gain or winter heat loss in the windows of the existing buildings.
54 At the same time, keeping the transparency of the window as high as possible is essential for decreasing
55 the lighting energy consumption during the daytime (Yang et al., 2017).

56
57 The research on VIPs has been applied in some fields to improve insulation performance. For
58 example, in some buildings, it can attain 5 times higher insulation values than traditional building insulating
59 materials (Fantucci et al., 2019). It has also been widely applied in vacuum cups and refrigerators (Thiessen
60 et al., 2018). A vacuum pipe has been applied in evacuated-tube solar collectors (Farid Arya et al., 2018).
61 The study of vacuum insulation technology, as applied to buildings, began in the 1990s. The VIP apparent
62 thermal conductivity ranges from 10 to 20% of that of conventional insulation materials such as glass wool,
63 expanded polystyrene, and polyurethane foam (Choi et al., 2016). The VIP consists of filler material and a
64 gas barrier envelope. The filler material has a porous structure with an open cell. This filler facilitates the
65 inner air evacuation. Different types of filler materials have been examined and tested in recent years (Choi
66 et al., 2016; Lee and Song, 2019; Liang et al., 2017; Paneri et al., 2019). For instance, (Kim et al., 2012b)
67 used phenolic foam as a filler material for a VIP. They concluded that the effective total thermal
68 conductivity of the VIP was approximately 5×10^{-3} W/m.K at a vacuum of 0.02 Pa, with 5% uncertainty in
69 the measurement. Moreover, the same research group experimentally evaluated the insulation ability of a
70 VIP with glass wool with a minimum centre-of-panel thermal conductivity of 1.2×10^{-3} W/m.K, and that of
71 opacified fumed silica with a minimum centre-of-panel thermal conductivity of 2.5×10^{-3} W/m.K, as fillers
72 at different pressing loads and pressure levels in (Kim and Song, 2013). Owing to the permeable open
73 structure of these types of fillers, they concluded that the VIP volume changes by the evacuation. In addition,
74 by applying the pressing load, the filler solid conduction increases, but the radiative thermal conductivity
75 decreases. Glass fibre is also used as the core material in a VIP for high-temperature applications in (Araki
76 et al., 2009). (Choi et al., 2016) proposed a new VIP consisting of two stainless steel plates, with pillar
77 support to sustain the atmospheric pressure. In their work, heat transfer and mechanical stability were
78 analysed together in the design stage. Then, to further decrease the conduction heat transfer through the

79 pillar, a multi-pass support (MPS) pillar with a cup-shaped holder was suggested and investigated. They
80 concluded that they attained a VIP with a very low effective thermal conductivity, i.e. approximately
81 1.18×10^{-3} W/m.K. In the recent investigations, the manufactured VIPs are proposed for insulating walls in
82 a building. These structures of VIPs are the most common, and provide an opaque view. Therefore, the light
83 transparency through the VIP was not a main concern. These structures consist of a metallized film barrier,
84 i.e. an "aluminium envelope placed inside the structure of a building wall".

85
86 Silica powder has been applied for the trial manufacture of VIPs. A silica aerogel with a thermal
87 conductivity of 2×10^{-2} W/m.K is usually used to make transparent VIPs (Buratti et al., 2017). It has been
88 found that using such material in smart windows decreases the U-values by 63% as compared to
89 conventional glass windows. In addition, a significant reduction in the light transmittance (by
90 approximately 30%) has been measured (Buratti et al., 2017). Moreover, the industrial production cost of a
91 VIP using silica aerogel remains very high. Hence, there is a need to search for another economically
92 competitive material.

93
94 Several trials for different filler materials have recently been investigated. Polyethylene
95 terephthalate (PET) film is applied via aluminium vapour deposition as a core material for analysis, and is
96 considered the core material of the metallic multilayer and overlapping fibre (Kim et al., 2012a). An
97 analysis of a heat transfer model for a nonporous silica vacuum insulation material was reported by
98 (Bouquerel et al., 2012a). Recently, Paneri et al., 2019 published a comprehensive review paper regarding
99 the materials used in transparent insulation panels. Based on this review, the authors concluded that an
100 aerogel quasi-homogeneous geometrical structure is an effective insulation material, achieving a centre-of-
101 panel U-value of 0.25 W/(m².K) with a thickness of 70 mm. However, the insulation cost of using silica
102 aerogels remains a challenging problem. Kwon et al., 2009 proposed powder-type, foam-type, and fibre-
103 type fillers, and then described a heat transfer model of the core material with a staggered beam. They
104 concluded that the fibre and staggered-beam thermal conductivities were lower than those of powder and
105 foam, owing to the longer thermal path. Johansson et al., 2012, proposed a short-term in situ performance
106 measurement of VIPs, and its accuracy is being verified. An outgassing problem from the VIP core material
107 and envelope was investigated in (Kwon et al., 2011) and reviewed in (Bouquerel et al., 2012b; Fricke et
108 al., 2008). The polymer fibre was also examined to analyse the reason for outgassing, as proposed by (Kwon
109 et al., 2011). In addition, the gas invasion from the film is described as a mass transfer model inside of the
110 film by (Bouquerel et al., 2012b).

111
112 Many numerical models and experimental methods have been used over the past several years to
113 evaluate the apparent thermal conductivity of VIPs with different core materials. Some of these consider
114 one-dimensional models (Baetens et al., 2010; Choi et al., 2016; Jung et al., 2014; Kwon et al., 2009), some
115 used two-dimensional models (Jang et al., 2011; Kim et al., 2012a; Lorenzati et al., 2016; Spagnol et al.,
116 2007), and a few other studies used 3D models (Fang et al., 2007; Johansson et al., 2012). Among these
117 investigations, pillar-supported VIPs are the most commonly investigated (F. Arya et al., 2018; Choi et al.,

118 2016), and these VIPs were applied for the walls of buildings. Therefore, they were not transparent VIPs.
119 Furthermore, the effects of changing the support structure are rarely addressed in the literature. In addition,
120 in most of the modelling methods, each component of the VIP effective thermal conductivity is determined
121 separately, and then the components are summed together. However, the coupling of the gas conduction,
122 vacuum region radiation, and the support structure conduction is very limited (Spagnol et al., 2007).
123 Therefore, the literature rarely discusses proposing different VIP core structures for transparent VIPs with
124 low thermal conductivity and competitive prices, as compared to silica aerogel panels and traditional
125 vacuum glazing insulations.

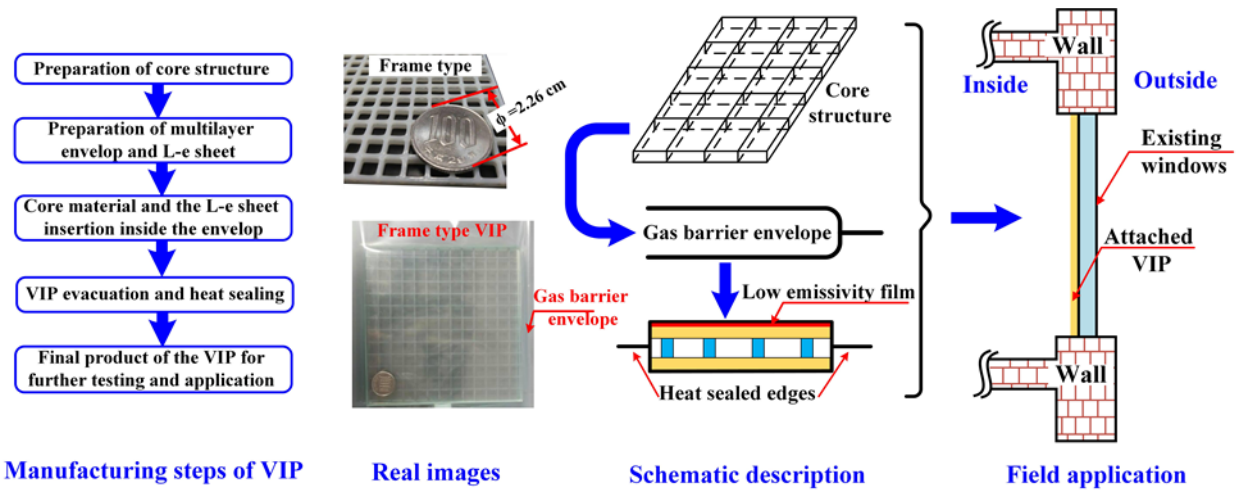
126 Based on the previous literature survey, this work aims to propose a new slim structured-core and
127 transparent insulation method for windows of existing buildings, with a lower cost than vacuum glazing
128 technology. Therefore, the originality of the present study is based on four main aspects. First, five distinct
129 designs for VIP spacer structures to retrofit the existing windows are conceived, manufactured, and
130 examined. The proposed VIPs are translucent and slim, and can be closely-fitted to the windows of existing
131 buildings by direct attachment. Second, new experimental methods that simultaneously evacuate and
132 measure the VIP thermal conductivity are used. Third, a 3D heat-transfer model is developed. This model
133 simultaneously solves all mechanisms of heat transfer existing in the VIP, including spacer bridge
134 conduction, vacuum gas conduction, and surface-to-surface radiation. This model allows us to evaluate the
135 contributions of all of the existing heat transfer mechanisms, which is essential for evaluating the conditions
136 at which each part could be the controlling parameter. Finally, annual estimations of building heat gain and
137 loss in two different hot and cold regions in Japan are respectively analysed for the five proposed VIP
138 designs. The types of VIPs investigated in this manuscript are very different from well-known conventional
139 VIPs, which have a solid core material structure and opaque aluminium foil or a metallized film barrier
140 envelope. The VIPs addressed in this manuscript have a hollow-frame structured-core material encapsulated
141 in a transparent multi-layered polymeric envelope; neither material is commonly used.

142

143 **2. Physical problem**

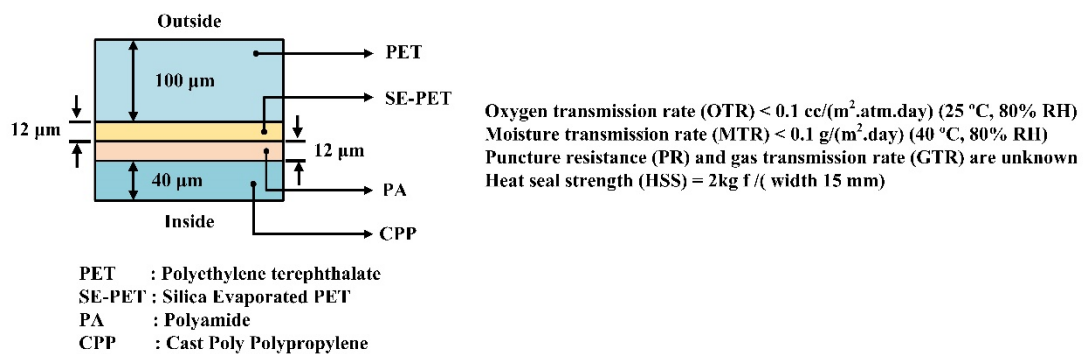
144 As mentioned above, a metallized film barrier envelope is commonly used in VIPs with solid core
145 materials for building insulations. This film is opaque, meaning that it cannot be applied to existing
146 windows. The appearance of vacuum glazing has generally solved this issue. However, these film barrier
147 envelopes have a relatively high cost and contribute less to retrofitting in buildings, owing to their single
148 purpose and very heavy weight. Therefore, this paper proposes five new designs of VIPs to be attached to
149 existing windows. A concept diagram of the proposed VIPs is shown in Fig. 1. The steps for the
150 manufacturing of the VIP are shown on the left side. The manufacturing steps start with the preparation of
151 the VIP core structure, low-emissivity (L-e) sheet, and transparent envelope. In this work, the heat sealing
152 of the envelope is a four-sided seal type. In addition, the L-e film is coated on one face for a measured
153 emissivity of 0.28, whereas the other face has a larger emissivity of 0.77. This type of L-e film is used
154 because for the same area, the single-face-coated L-e film has a lower price as compared to the two-sided
155 coated film. Therefore, it contributes to lowering the total cost of the VIP. In this work, the L-e side is
156 directed to the vacuum space. This structure decreases the contribution of the radiation heat transfer, which

157 is the dominant factor at very low-pressure levels (as will be discussed later). The core structure and the L-
 158 e film are inserted in a transparent gas barrier envelope. The transparent envelope facilitates the
 159 applicability of these VIPs to existing windows where light transparency is indispensable. The full structure
 160 is evacuated and sealed in a vacuum sealing machine after reaching the vacuum design pressure. The real
 161 photos, schematic representation, and the field applications of the VIPs are depicted in Fig. 1 from the left
 162 to the right of the figure. The proposed VIPs could assist in enhancing the insulation ability of existing
 163 windows, with light transparency. In addition, the proposed VIPs can be considered as thermal-insulating
 164 transparent curtains.



165 **Manufacturing steps of VIP** **Real images** **Schematic description** **Field application**
 166 Fig. 1 Manufacturing steps, real images, schematic description, and the proposed real field application of
 167 the structured-core and transparent vacuum insulation panel (VIP) for existing windows.

168 The current VIPs are carefully designed for light transparency requirements. For instance, a transparent
 169 gas barrier film is applied as a covering envelope for the structured core. This envelope is favourable for
 170 sealing and transparency. The detailed structure and dimensions of the gas barrier envelope are depicted in
 171 Fig. 2.



172
 173 Fig. 2 Detailed structure of the transparent gas barrier envelope used in the present work with properties
 174 essential for VIP life cycle analysis.

175
 176 In this study, the insulation performance is implemented for five different designs of structured-core and
 177 transparent VIPs, as shown in Fig. 3. These VIP designs include a peek spacer, mesh spacer, frame
 178 spacer, modified peek spacer, and silica aerogel spacer. All of these VIPs are designed,

179 manufactured, and experimentally-tested, except for the modified peek spacer. The modified peek
 180 spacer and another cylindrical pillar are proposed as extensions for the peek spacer. Therefore, the
 181 experiment will be conducted for the peek spacer and validated with a numerical model, and the
 182 same numerical model and solution methods will be applied for the modified peek spacers and
 183 cylindrical pillar. The modified peek spacer, peek spacer, and cylindrical pillar will be compared
 184 together to highlight methods for decreasing the conduction heat flux in pillar-supported VIPs.

185
 186 Before discussing the design details of the structured-core and transparent VIPs used in this work, it is
 187 worth mentioning that at low pressures, the gas conduction is very small, and the effects of gas convection
 188 can be neglected (Choi et al., 2016; Fang et al., 2007; Memon et al., 2019a). The dominant parameters that
 189 can be controlled to decrease the effective thermal conductivity of a VIP in low-pressure conditions are the
 190 radiation heat transfer and the thermal bridges through the outside frame and inner core structure. Therefore,
 191 to enhance the VIP insulation performance, this work decreases the radiation by implementing the L-e film.
 192 In contrast, the heat conduction through the support structure is decreased by changing the core structure
 193 from a common solid core structure to hollow-designed core structures, as depicted in Fig. 3.

194 As shown in Fig. 3, a peek spacer is a modified design of a cylindrical pillar-supported VIP. A
 195 conventional pillar-supported VIP uses a continuous cylindrical cross-section pillar with a diameter of (D).
 196 This design is the most widespread in the literature, and is used for vacuum glazing technology (Fang et al.,
 197 2010). However, the peek design differs from the existing structures, as it decreases the diameter of the
 198 pillar to (d) while maintaining the pillar diameter head as (D). This decreases the space occupied by the
 199 pillar, and slightly enhances the light transparency. In addition, it is possible to attain a decrease in the pillar
 200 thermal bridge. To further utilise the same idea, a modified peek pillar-supported VIP is proposed. In this
 201 type of pillar-supported VIP, a semi-spherical head is used for the pillar. In such a case, the connection
 202 between the hot side and cold side can be reduced, and the thermal bridges through the pillars can be further
 203 decreased. In the pillar-supported VIPs in this work, i.e. peek and modified peek, an acrylic plate with $\delta=$
 204 1 mm is used to fix the pillars inside it. In addition, other two acrylic plates with δ of 1 mm each are used
 205 to keep the vacuum space at one plate, with a thickness of δ at each side. In these two cases, a vacuum
 206 space can be obtained, with a thickness of $H_v= 1.5$ mm. Therefore, the total thickness of the pillar-supported
 207 VIPs (with the peek spacer or modified peek spacer) in this study is 4.5 mm. The pillars are fabricated from
 208 polycarbonate with a thermal conductivity of 0.2 W/m.K (Choi et al., 2016). The detailed dimensions of
 209 the VIPs are provided in Table 1.

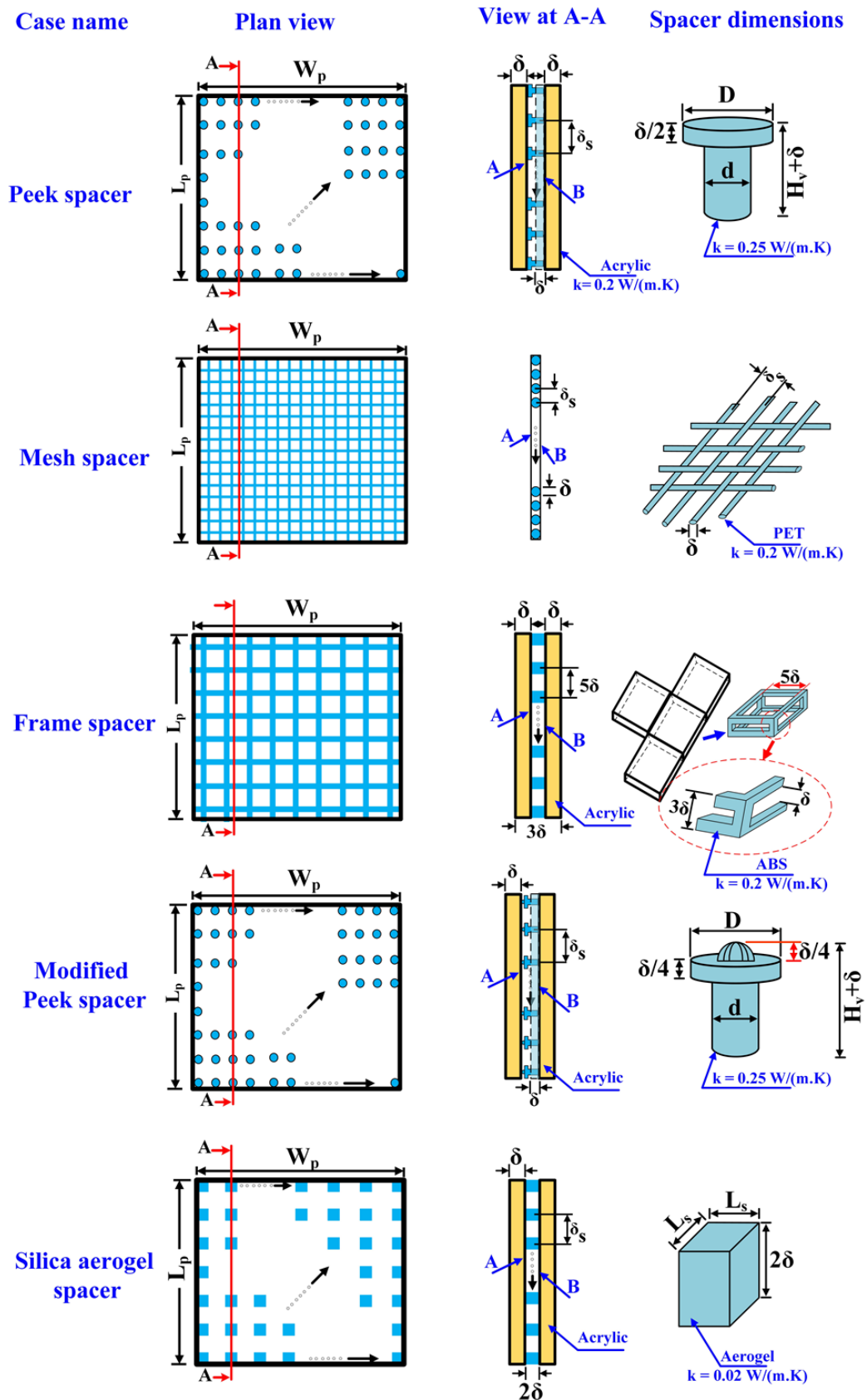
210

211 Table 1: Detailed dimensions of the current structured-core and transparent vacuum insulation panels
 212 (VIPs).

Dimension	Value (mm)	Dimension	Value (mm)
δ	1	D	1.8
W_p	150	L_p	150
d	1.2	H_v	1.5
δ_s	10	L_s	5

213

214 To further decrease the thermal bridges through the spacer structure, a mesh-type spacer is proposed, as
215 shown in Fig. 3. The mesh-type spacer consists of an equal-squares mesh fabricated by the sewing of
216 circular polycarbonate rods, each with diameter $\delta=1$ mm. This approach decreases the connection area
217 between every two rods to just a point. Thus, the heat transfer by conduction can be lowered, owing to the
218 significant reduction in the connection area. In this case of the VIP, the total thickness of the panel is 2 mm.
219 The main advantages of this design are an easier fabrication process and a slim appearance. As shown in
220 Fig. 3, the frame-type spacer uses two 3D printed frames that have a uniform thickness throughout and are
221 spaced by rectangular pillar supports. In the top layer of the frame, the pillars are 3D-printed and
222 compressed to the lower frame. The total thickness of this panel is approximately 3 mm, and no acrylic
223 plates are used to keep the vacuum space, as in the case of pillar-supported VIPs. Finally, as a reference
224 case, a common transparent VIP uses silica aerogel spacers. Therefore, a silica aerogel spacer with
225 dimensions of $L_s=2.5$ mm and a thermal conductivity of 0.02 W/m.K is used between two acrylic plates
226 with 1 mm thickness each. The space between the two consecutive spacers is designed based on a deflection
227 analysis developed by the author in a previous work (Yang et al., 2017). Therefore the δ_s used in this work
228 is 10 mm, to maintain the deflection between the two consecutive supports less than 0.5 mm (Yang et al.,
229 2017).



230

231

232

233

Fig. 3 Concept diagram of the proposed structured-core and transparent VIPs with different core structures of peek spacer, mesh spacer, frame spacer, modified peek spacer, and silica aerogel spacers.

234 **3. Experimental setup**

235 Four experimental setups are established to produce and measure the relevant characteristics of the
236 current structured-core and transparent VIPs. The first setup is used to measure the emissivity of the L-e
237 coated film. The second setup is used for the production process of low-pressure VIPs, with simultaneous
238 measurement of the panel thermal conductivity at different pressure levels. In the third experimental setup,
239 four-trial production methods for the VIPs are compared. In the last setup, a light transparency test is
240 conducted to evaluate the transparency of the proposed VIPs. All of the experimental setups are discussed
241 in detail in the following sections.

242

243 **3.1. Measurements of the emissivity of the L-e film**

244 The cost of a single-face coated L-e film represents approximately 50% of the total cost of the VIP. This
245 cost increases to approximately 65% in the case of using a double-face coated L-e film. Therefore, to keep
246 the proposed VIPs cost-effective for smart windows, a single-face coated L-e film is used. In this type of
247 L-e film, the emissivity of each face is different. In addition, it is essential to keep the L-e side oriented to
248 the inside of the vacuum space. In view of this, an evaluation of the real emissivity value of the L-e film is
249 essential for developing a thermal model. Consequently, an experiment is conducted to define the coated
250 surface, and to measure the real emissivity of each side. The measurement is performed using an
251 emissometer with a scaling digital voltmeter (Model AE1 RD1). This setup consists of a detector, finned
252 heat sink, scaling digital voltmeter, and device power supply. A real photo of the setup and the schematic
253 layout are depicted in Figs. 4-a and b, respectively. The detector portion is electrically heated. A finned heat
254 sink is provided with the device to keep both a calibration standard and the L-e film at the same temperature.
255 The scaling digital voltmeter is used to monitor the measured sample emissivity. Before conducting each
256 experiment, a calibration is performed by using the standard emissive sample provided with the device. The
257 measurement begins with the calibration step. In this step, a calibration standard sample with a known
258 emissivity of 0.88 is inserted between the detector and the heat sink. Then, a variable resistance is manually
259 changed, until reaching the exact emissivity of the standard sample. After that, the standard calibrated
260 sample is replaced with the L-e film. After reaching a steady state condition, the emissivity of the film side
261 facing the detector can be measured. The same step is repeated for the other face of the film. In the current
262 experiments, the emissivities of the two sides of the film are approximately 0.28 and 0.77, respectively.

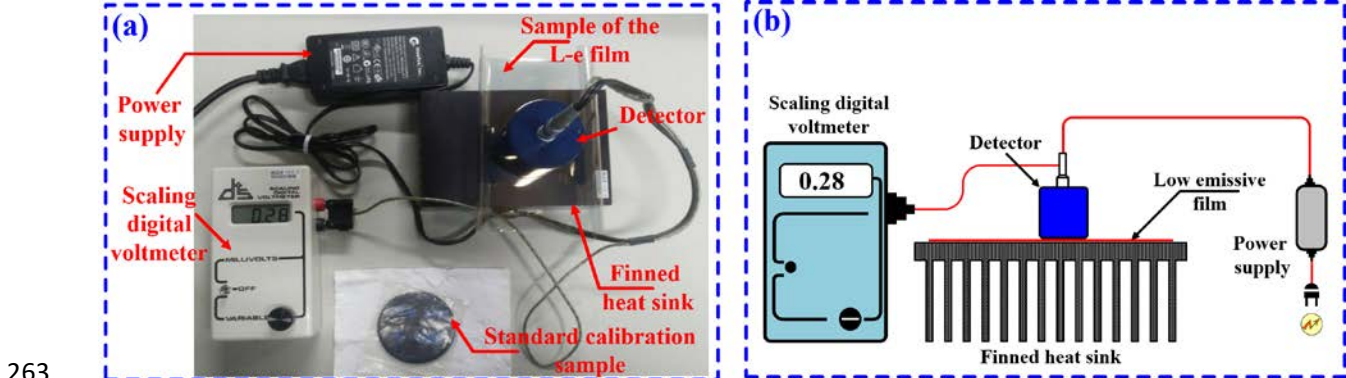


Fig. 4 Experimental setup for the measurement of the film real emissivity; (a) real photograph and (b) schematic representation of the setup.

266 **3.2. Development of the vacuum insulation panel (VIP) and measurement of the effective thermal**
267 **conductivity**

268 Initially, two vacuum methods are used to produce the VIP. The first system uses a lab-scale vacuum
269 sealing machine. In this machine, the pressure level can be controlled either automatically or manually.
270 After reaching the desired pressure, sealing is automatically performed. Then, the sample can be taken from
271 the vacuum chamber and used for further testing. This sealing machine consists of buster and rotary vacuum
272 pumps connected in series. A sealing width of 9 mm can be achieved using such a machine. This large
273 sealing width prevents the penetration of atmospheric pressure, as compared with conventional sealing
274 methods with a sealing width of 4 mm. However, the controlled pressure is the machine chamber pressure.
275 Moreover, the chamber pressure is slightly different than the real pressure inside the VIP after the sealing.
276 This is because after the sealing is made, the pressure inside the VIP starts to increase, owing to outgassing
277 from the core material, and other factors as explained in (Kwon et al., 2011) and discussed in the results
278 section.

279
280 In contrast, the new measurement method applied herein is used to keep the pressure inside the VIP
281 nearly constant during the thermal conductivity measurement. This method simultaneously accomplishes
282 evacuation and thermal conductivity measurement. In this system, another small-scale vacuum system is
283 connected to the heat flow meter (HFM) apparatus. Three sides of the envelope are thermally sealed after
284 inserting the VIP core structure and the L-e film. The sealing is performed using the vacuum sealing
285 machine, with a sealing width of 9 mm. Then, the last side of the envelope is kept open to be connected to
286 a small-scale vacuum system using a hose/pipe, as shown in Fig. 5. The schematic apparatus and a real
287 photo of the simultaneous evacuation thermal conductivity measurements are depicted in Figs. 5-a and b,
288 respectively. The vacuum system in this experiment consists of a reciprocating vacuum pump and a dry-
289 type turbomolecular vacuum pump connected in series. For the measurement of pressure, a Pirani pressure
290 gauge with a pressure display unit is connected at the inlet of the VIP. The VIP with the pressure
291 measurement device can be isolated from the evacuation system using a valve. First, the reciprocating pump
292 is used to lower the pressure inside the VIP to approximately 20 Pa. After that, the turbomolecular pump is
293 used to further decrease the pressure to the desired value. A dry-type or oil-free turbomolecular pump is
294 favourable for such applications, as recommended by (Memon et al., 2019b). The pressure sensor is located
295 as closely as possible to the VIP, to measure the approximate pressure inside the VIP. After reaching the
296 desired vacuum level, the VIP sample is inserted into the HFM apparatus. In this apparatus, the temperature
297 of the hot and cold sides of the VIP can be controlled by using the controlling unit, either from the controller
298 interface, or via system software on a PC. The steady-state hot- and cold-side temperatures of the HFM are
299 kept constant at 35.5 °C and 10.5 °C, respectively, during all of the tests. The instrument also has a facility
300 for measuring the total thickness of the sample. The HFM has two heat flux sensors for accurate
301 measurements of the heat fluxes, one on each side of the VIP. After reaching the steady-state criteria with
302 a change in the measured heat fluxes of approximately 2%, the measured sample thermal conductivity,
303 thickness, walls temperature, sample mean temperature, and heat flux values are automatically displayed
304 on the meter interface, and are transmitted to the meter software on the PC and recorded.

305
 306 The effective thermal conductivity of the VIP is measured based on a Fourier equation of one-
 307 dimensional heat conduction, as given in the manufacturing datasheet of the HFM apparatus:

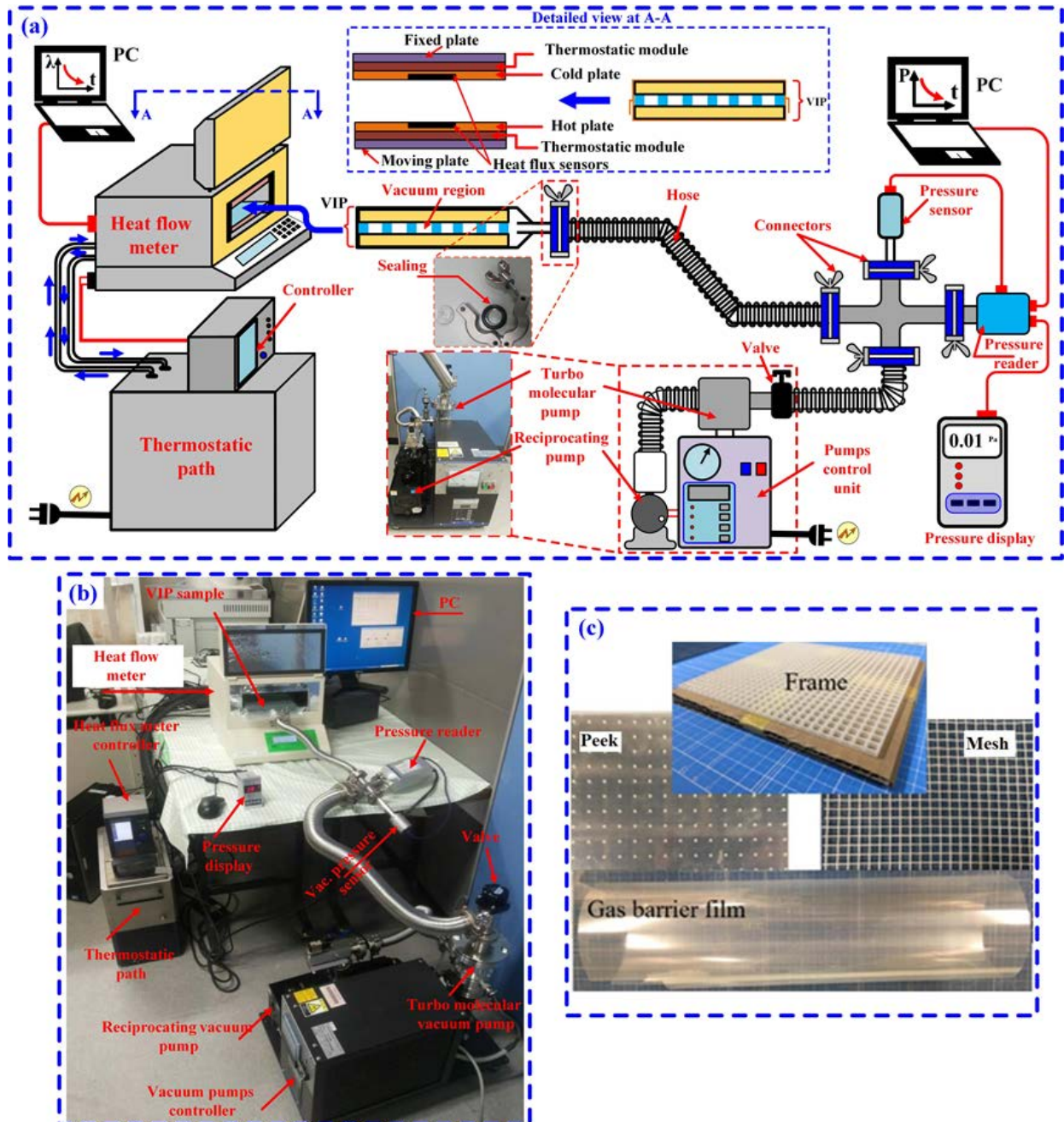
$$308 \quad \lambda_{eff,exp} = \left(\frac{q_h + q_c}{2} \right) \times \frac{L_v}{\Delta T} \quad (1)$$

309 Here, $\lambda_{eff,exp}$, q_h , q_c , l_v , and ΔT are the effective measured thermal conductivity of the VIP (in W/m.K),
 310 the measured heat flux on the hot and cold sides of the sample using the heat flux sensors (in W/m²), the
 311 measured VIP thickness (in m), and the temperature difference on the sides of the sample (in °C),
 312 respectively. In this work, the thermal conductivity is measured for all of the VIPs, except for the modified
 313 peek spacers (which are numerically investigated, and are not manufactured). The technical specifications
 314 of the measuring tools and their accuracies are depicted in Table 2.

315 Table 2 Technical specifications of the instruments used in the thermal conductivity measurements.

Instrument	Technical specifications	
Heat flow meter (HFM) apparatus	Model No	HC-074
	Accuracy	≤ 1%
	Repeatability	0.2%
	Hot plate temperature range	5 °C to 75 °C
	Cold plate temperature range	-20 °C to 50 °C
	Thermal conductivity range	0.005 to 0.8 W/m.K
Pirani gauge	Model No	ST2-1
	Pressure range	10 ⁻⁵ to 10 ⁻³ Pa
	Accuracy	±10% when 10 ⁻⁵ ≤ P < 3 Pa ±15% when 3 ≤ P ≤ 10 Pa

316

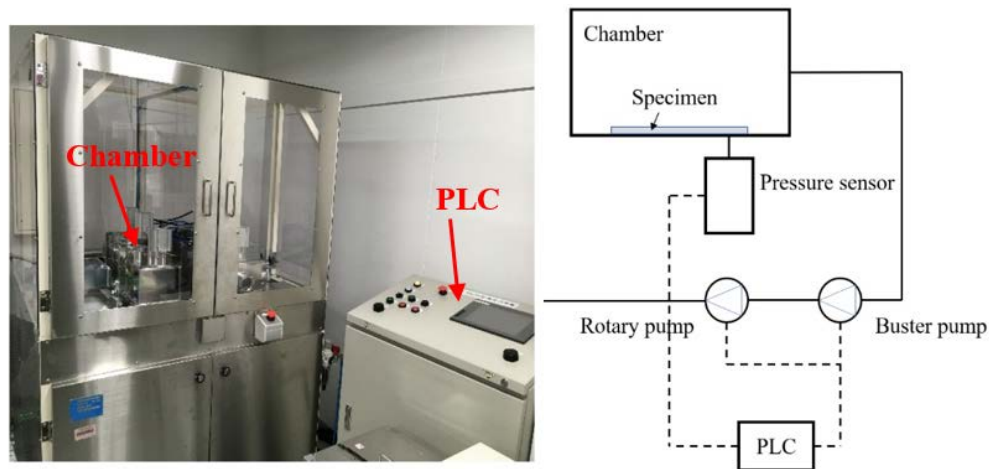


317
 318 Fig. 5 Detailed experimental setup used for the evaluation of the centre-of-panel thermal conductivity
 319 (a) schematic representation of the setup, (b) real photo of the experimental apparatus, and (c) real
 320 photo of peek, frame, and mesh VIPs with the gas barrier film.
 321

322 3.3. Experimental methods for the trial production of the VIP

323 Before conducting the experiment presented in Section 3.2, a lab-scale vacuum sealing machine, as seen
 324 in Fig. 6, is used for the evacuation and sealing. In this setup, the sample inside the vacuum chamber is
 325 connected to the Pirani gauge to measure the pressure inside the VIP. However, it was found that after the
 326 sealing was performed, the inside pressure of the VIP increased from 0.24 Pa to 1.15 Pa in 10 minutes for
 327 the frame-type VIP. This is attributed to the outgassing from the core material and the sealed edges of the
 328 envelope (Kwon et al., 2011). In that regard, to measure the VIP thermal conductivity, it is essential to

329 perform the evacuation and the sealing, and then to subsequently transfer the sample to the measuring HFM
330 apparatus. In this case, with the outgassing from the core structure, the estimation of the exact inner pressure
331 of the VIP is very difficult.



332
333 Fig. 6 Photograph and schematic of the vacuum sealing equipment.

334 To avoid this difficulty, four different methods are used and compared for the trial production of the
335 frame-type VIP as examples, using the experimental setup shown in Fig. 6. The main purpose of these steps
336 is to compare the thermal conductivity variations of the VIP with different production methods.

337
338 In these methods, outgassing from the core structure is minimised in different ways. In the first setup,
339 Fig. 7-a, **named the "normal case"**, the VIP is manufactured using the vacuum sealing machine in Fig. 6,
340 and a calcium oxide adsorbent pack is used to minimise the outgassing from the core material. In the second
341 setup in Fig. 7-b, **named "vacuum drying with N₂"**, the VIP structure is kept inside an environmentally-
342 controlled unit. In this unit, the environmental temperature is maintained at 70 °C for 24 h, and the structure
343 is connected to the vacuum machine to maintain the pressure at 0.1 Pa. This method is used to release the
344 outgassing from the core structure. Then, nitrogen is supplied to the inside of the environmentally-
345 controlled unit. After that, nitrogen is exhausted from the unit. Then, the VIP structure is evacuated and
346 sealed using the vacuum sealing machine.

347
348 In the third setup, Fig. 7-c, **named "heating"**, a new step is proposed to reduce the time for the VIP
349 production process. In this setup, the two flat silicon rubber heaters are used to heat up the VIP during the
350 evacuation. This also could help the outgassing of the water vapour from the inside of the core structure.
351 The heaters are temperature-controlled using a temperature controller, to maintain the temperature of the
352 VIP at 70 °C during the evacuation. In the second and the third trial methods, calcium oxide adsorbent
353 packs are also used. Finally, in the fourth production method in Fig. 7-d, **named "gas adsorbent getter"**,
354 an absorbent material that contains calcium oxide and alloy getter is inserted into the VIP. The calcium
355 oxide absorbs the water vapour, while the alloy getter absorbs other gases such as nitrogen and carbon
356 dioxide. Consequently, the pressure rise owing to the outgassing can be reduced. The results of these four
357 trial manufacturing methods are compared in detail in Section 5.2.

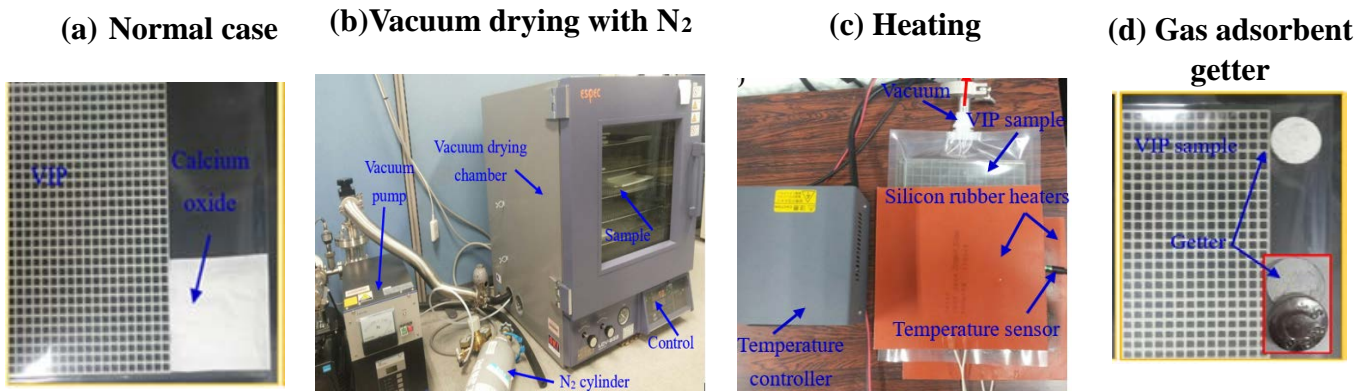
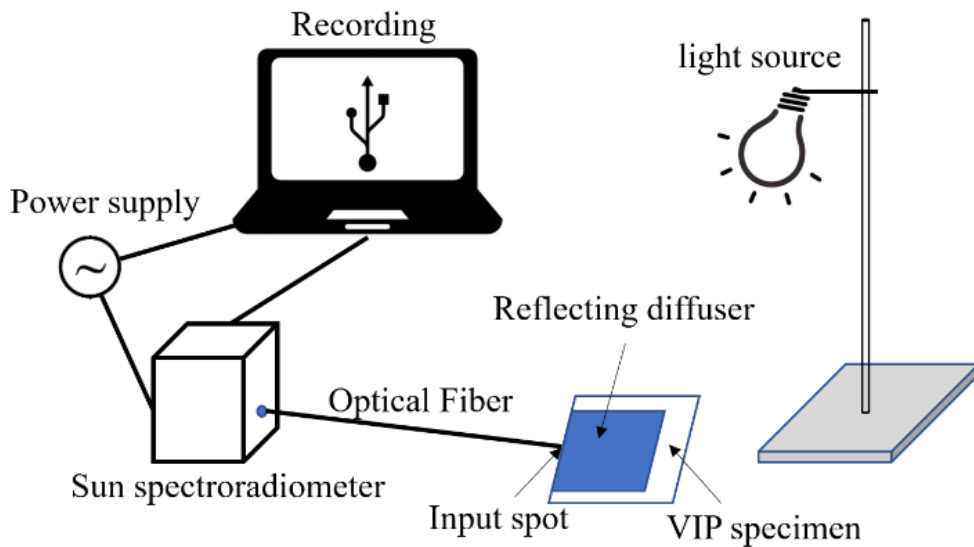


Fig. 7 Trial manufacturing methods for the frame-type VIP (a) normal method with calcium oxide adsorbent, (b) using vacuum drying chamber with N_2 , (c) using flat silicon rubber heaters during the evacuation, and (d) using gas adsorbent getter.

358 **3.4. Experimental measurements of the structured-core VIP transparency**

359 The schematic for light transparency measurement is depicted in Fig. 8. In this setup, the translucent VIP
 360 specimen is placed on a reflection diffuser, and is irradiated by an incandescent light source. The light
 361 source wavelength is measured to be at 800 nm (the maximum range for the visible wavelength), and the
 362 illuminance is measured with intensity in $\mu W / (cm^2 \cdot nm)$, with and without VIP shading. The transparency
 363 ratio is defined as the ratio between the transmitted intensity in the case of using the VIP to the transmitted
 364 intensity in the case without the VIP.



365
 366

Fig. 8 Schematic of illuminance measurement.

367 4. Theoretical analysis

368 In VIPs, the inner pressure must be reduced to below 10 Pa. Increasing the gas pressure above this value
369 rapidly increases the VIP thermal conductivity (Baetens et al., 2010). In addition, the total heat transfer in
370 VIPs can be divided into four parts: radiation heat transfer through the vacuum space, heat conduction
371 through the skeleton of the core of the core structure, gas conduction, and gas convection (Baetens et al.,
372 2010). To enhance the insulation performance of the VIP, all of these parts must be minimised. However,
373 at very low pressures, the convection can be naturally converted to pure gas conduction. Therefore, the
374 convection can be ignored in the calculation (F. Arya et al., 2018; Choi et al., 2016). The basic governing
375 equations used in this study are the 3D heat conduction equation, coupled with the surface-to-surface
376 radiation model. For steady-state 3D heat conduction with a source term, "ANSYS FLUENT" solves the
377 energy equation in the following form ("ANSYS FLUENT Theory Guide," 2011):

$$378 \quad \nabla \cdot (k \nabla T) + S = 0 \quad (2)$$

379 In the above, T is the temperature, k is the element thermal conductivity, and S is a source term added to
380 consider the effect of radiation in the vacuum space ("ANSYS FLUENT Theory Guide," 2011). This
381 equation is solved to obtain the temperature distribution and heat transfer rate through the solid layers,
382 including the hot and cold plates' conduction and the inner structure, but without a radiation heat source.
383 To include gas conduction in the vacuum layer, the same equation (with the radiation source term) is solved,
384 but with the gas thermal conductivity at the designed pressure.

385 Air thermal conductivity is a function of the pressure and pore size (Baetens et al., 2010). This results
386 from the exact inverse relationship between the gas pressure and the molecule-molecule collisions' mean
387 free path. In more detail, as the gas pressure is decreased, the number of gas molecules available to transport
388 heat is proportionally decreased. Thus, a substantial reduction in heat transfer caused by gaseous conduction
389 occurs at low-pressure levels. To neglect gaseous conduction, the pressure within the vacuum space must
390 be less than 0.1 Pa (Collins and Simko, 1998). The air thermal conductivity, λ_v , in W/m.K, at different
391 pressures and pore sizes, is calculated as follows (Kim and Song, 2013):

$$392 \quad \lambda_v = \frac{\lambda_o}{1 + \frac{(1.07 \times 10^{-7})T}{l_v P}} \quad (3)$$

393 Here, T , l_v , and P are the temperature in K, vacuum thickness in m, and gas pressure in Pa, respectively.
394 In addition, λ_o is the air thermal conductivity at room temperature and pressure. In this study, it is taken as
395 0.026 W/m.K. However, the vacuum thickness for the proposed structures changes in some locations. To
396 incorporate this into the numerical calculations, a multi-zone approach is used. In this approach, every
397 vacuum space with the same thickness is defined as a specific zone. Using this idea, the thermal
398 conductivity of each zone can be calculated by knowing the thickness of the vacuum space between the hot
399 and cold plates. For example, in frame-type spacers as seen in Fig. 9, the vacuum thicknesses in zone-1 and
400 zone-2 are 3 mm and 1 mm, respectively. Therefore, the thermal conductivities of the respective vacuum
401 spaces in these two zones are considered to be different. The same idea is also applied for all proposed core
402 structures where this issue exists.

403

404 Three different techniques exist in the literature for considering the contribution of the radiation heat
 405 transfer in the vacuum space. In all of these models, an equivalent thermal conductance is calculated. This
 406 thermal conductance is dependent on the emissivity of the hot and cold sides of the VIP, and the view factor.
 407 In this case, Equation (2) is solved, without the source term. However, the vacuum space thermal
 408 conductivity is modified to include the effect of radiation. In the first technique, the equivalent radiation
 409 conductance through the vacuum space is estimated using the following correlation (Fang et al., 2009):

$$410 \quad C_{h-c,radiation,1} = 4\varepsilon_{eff}\sigma T_{avg}^3 \quad (4)$$

411 In Equation (4), $C_{h-c,radiation,1}$, ε_{eff} , σ , and T_{avg} are the equivalent radiation conductance between the hot and
 412 the cold sides of the VIP in units of $W/m^2.K.$, the effective emittance of the hot and cold sides of the vacuum
 413 space, a Stefan–Boltzmann constant in $W/m^2.K^4$, and the average temperature of the vacuum space in
 414 Kelvin, respectively. The effective emittance is calculated as follows (Fang et al., 2009):

$$415 \quad \frac{1}{\varepsilon_{eff}} = \frac{1}{\varepsilon_h} + \frac{1}{\varepsilon_c} - 1 \quad (5)$$

416 Here, ε_h and ε_c are the emissivities of the hot and cold sides of the VIP, respectively.

417 In the second technique, the radiation contribution is calculated based on the principle of the heat exchange
 418 between two parallel surfaces separated by a very small gap (Incropera et al., 2007):

$$419 \quad Q_{rad} = \frac{\sigma(T_h^4 - T_c^4)}{\left(\frac{1 - \varepsilon_h}{A_v \varepsilon_h}\right) + \left(\frac{1}{A_v F_{h-c}}\right) + \left(\frac{1 - \varepsilon_c}{A_v \varepsilon_c}\right)} = \frac{\sigma A_v (T_h^4 - T_c^4)}{\left(\frac{1 - \varepsilon_h}{\varepsilon_h}\right) + \left(\frac{1}{F_{h-c}}\right) + \left(\frac{1 - \varepsilon_c}{\varepsilon_c}\right)} \quad (6)$$

420 In the above, F_{h-c} is the view factor between the hot and cold surfaces, and A_v is the surface area of the
 421 panel facing either the hot or the cold side of the vacuum space, in m^2 . For a unity view factor, the equivalent
 422 thermal conductance owing to the radiation is calculated as following (Incropera et al., 2007):

$$423 \quad A_v C_{h-c,radiation} (T_h - T_c) = \frac{\sigma A_v (T_h^4 - T_c^4)}{\left(\frac{1}{\varepsilon_h} - 1\right) + 1 + \left(\frac{1}{\varepsilon_c} - 1\right)} \quad (7)$$

$$424 \quad C_{h-c,radiation,2} = \left(\frac{\sigma(T_h^4 - T_c^4)}{\left(\frac{1}{\varepsilon_h}\right) + \left(\frac{1}{\varepsilon_c}\right) - 1} \right) / (T_h - T_c) \quad (8)$$

425 Lastly, in the third technique, the following correlation is used for the prediction of the value of
 426 $C_{h-c,radiation}$ as follows (Yang et al., 2018):

$$427 \quad C_{h-c,radiation,3} = \varepsilon_h \varepsilon_c C_b \left\{ \left(\frac{T_h}{100}\right)^4 - \left(\frac{T_c}{100}\right)^4 \right\} \frac{1}{(T_h - T_c)} \quad (9)$$

428 In that regard, C_b is a black body radiation constant factor, and it is set to 5.67, as proposed by (Yang et al.,
 429 2018). After the thermal conductance owing to the radiation is evaluated, the increase in the vacuum space
 430 thermal conductivity owing to the radiation effect can be estimated by multiplication of the calculated C_{h-}
 431 $c,radiation$ by the vacuum layer thickness. Therefore, the new thermal conductivity of the vacuum space,
 432 considering both the radiation effect and gas conduction effect, can be calculated as follows (Choi et al.,
 433 2016):

$$434 \quad \lambda_{v, gas\ conduction+radiation} = \lambda_v + C_{h-c,radiation} l_v \quad (10)$$

435 Moreover, the contribution of the radiation heat transfer rate, Q_{rad} , in watts between the two sides of the
436 VIP is calculated using the following correlation (Fang et al., 2010):

$$437 \quad Q_{rad} = A_v C_{h-c, radiation} (T_h - T_c) \quad (11)$$

438 Throughout of all these three models, the view factor between the hot and cold walls is set as unity. This is
439 because of the smaller gap and larger facing area between the hot and cold sides of the VIP.

440
441 In the present study, a new modelling method is used to predict the contribution of the radiation effect
442 between the hot and cold sides of the VIP. This method couples the conduction heat transfer through the
443 vacuum space and support structure with the surface-to-surface (S-S) radiation model in the vacuum space.
444 This model is implemented in the commercial ANSYS software (“ANSYS FLUENT Theory Guide,” 2011).
445 The model solves Equation (2) for the vacuum space, so as to include the conduction and the radiation. This
446 model also calculates the view factor for all contributing surfaces in the computational domain and in
447 contact with the vacuum space. In the S-S model, the energy exchange between two surfaces depends on
448 their size, orientation, and separation distance, which are used to calculate the view factor. These parameters
449 are calculated automatically from the design geometry of the VIP imported by the Fluent module. This
450 model assumes that any emission, absorption, or radiation scattering by the vacuum domain are ignored.
451 Consequently, only the radiation from “surface-to-surface” is considered. In addition, the model assumes
452 that the surfaces' emissivities are independent of the wavelength. This model also can be used for solar
453 collectors' applications, radiative space heaters, and heat rejection methods in aircraft (“ANSYS FLUENT
454 Theory Guide,” 2011). This model simultaneously solves the radiation exchange equation with the energy
455 equation of the solid regions and the gas conduction in the vacuum space by the use of the source term for
456 radiation, as explained in detail in the ANSYS theory guide (“ANSYS FLUENT Theory Guide,” 2011).
457 The model results are compared with the results of previous methods in the literature in the model
458 verification step.

459
460 In the (S-S) model, the energy flux leaving a certain surface consists of the directly-emitted energy and
461 the reflected energy. The emitted part depends on the surface emittance. However, the reflected part depends
462 on the incident energy flux coming from the surroundings. The last part can be considered in terms of the
463 flux of the energy leaving all other surfaces. Therefore, the energy flux leaving from a certain surface k in
464 the VIP domain, $q_{out,k}$, can be written as follows:

$$465 \quad q_{out,k} = \varepsilon_k \sigma T_k^4 + \rho_k q_{in,k} \quad (12)$$

466 In Equation (12), ε_k , T_k , ρ_k , and $q_{in,k}$ are the emissivity, absolute temperature, the reflectivity of the surface
467 k , and the flux of energy incident from all other surfaces and received by the surface k , respectively.
468 According to the grey-body model, the surface absorptivity is assumed to be the same as the surface
469 emissivity. The amount of incident energy flux on the surface k from another surface(s) j is calculated as a
470 direct function of the view factor between the surface k and the surface(s) j . Therefore, the incident flux of
471 energy on the surface k can be calculated as follows:

472
$$q_{in,k} = \frac{1}{A_k} \sum_{j=1}^N A_j q_{out,j} F_{j-k} \quad (13)$$

473 Here, A_k , A_j , and F_{j-k} are the area of the surfaces k and j , and the view factor between the surface j and
 474 surface k , respectively. In addition, N is the total number of surfaces participating in the radiation. This
 475 number could also include the surface k if the view factor between the surface k and itself is not zero. The
 476 reciprocity relationship for the view factor calculation gives the following:

477
$$A_k F_{k-j} = A_j F_{j-k} \quad \text{for } j = 1, 2, 3, \dots \dots N \quad (14)$$

478 Substituting in Equation (13), then $q_{in,k}$ can be calculated as follows:

479
$$q_{in,k} = \sum_{j=1}^N q_{out,j} F_{k-j} \quad (15)$$

480 Therefore, Equation (12) changes to the following:

481
$$q_{out,k} = \varepsilon_k \sigma T_k^4 + \rho_k \sum_{j=1}^N q_{out,j} F_{k-j} \quad (16)$$

482 This equation can be written as follows:

483
$$J_k = E_k + \rho_k \sum_{j=1}^N J_j F_{k-j} \quad (17)$$

484 Here, J_k is the radiant energy that is given off surface k , and is known as radiosity, and E_k represents the
 485 emissive power of the surface k . This equation can be mathematically represented in matrix form as
 486 follows:

487
$$KJ = E \quad (18)$$

488 In the above, K is a matrix with $N \times N$ dimensions; J and E are the radiosity and emissive power vectors
 489 with length N each, respectively. The view factors between the participating surfaces must be calculated
 490 first to obtain the radiosity matrix. Therefore, after importing the design of the VIP core structure, the
 491 surfaces' orientations, areas, and spacing are calculated. Then, the view factors for all of the participating
 492 surfaces are calculated using the following relationship (“ANSYS FLUENT Theory Guide,” 2011).:

493
$$F_{k-j} = \frac{1}{A_k} \int_{A_k} \int_{A_j} \frac{\cos \theta_k \cos \theta_j}{\pi r^2} \delta_{kj} dA_k dA_j \quad (19)$$

494 Here, δ_{kj} is calculated by the visibility of dA_j to dA_k , and the value of δ_{kj} equals unity if dA_j is visible to
 495 dA_k , and zero otherwise. Small-scale computational domains, boundary conditions, and mesh details are
 496 depicted in Fig. 9. This step is used to compare the computationally-estimated centre-of-panel thermal
 497 conductivity with the experimental results, and to evaluate the contribution of each heat transfer mode.
 498 Finally, after a solution convergence with a residual of less than 1×10^{-10} in the energy equation is attained,
 499 the centre-of-panel thermal conductivity is numerically estimated as follows:

500
$$k_{eff,num.} = (q_{total}) \times \frac{L_v}{(T_h - T_c)} \quad (20)$$

501 In Equation (20), $K_{eff,num}$ and q_{total} are the numerical estimated centre-of-panel thermal conductivity and the
502 area weighted average of the total heat flux on the hot side. The latter equals that on the cold side at the
503 converged steady-state condition, and is estimated as follows (“ANSYS FLUENT Theory Guide,” 2011):

$$504 \quad q_{total} = \frac{1}{A} \int q \, dA = \frac{1}{A} \sum_{i=1}^n q_i |A_i| \quad (21)$$

505 Here, n is the total number of elements in the selected area.

506

507 **4.1. Boundary conditions**

508 To solve the model-governing equations, one or more boundary conditions must be used. Therefore, Fig.
509 9 depicts a schematic representation of the boundary conditions used for all proposed core-structured VIPs.
510 In more detail, to evaluate the centre-of-panel thermal conductivity, one side of the panel is maintained at
511 a hot temperature of 35.5 °C, while the other side is kept at a cold temperature of 10.5 °C. The wall
512 emissivity and temperature are defined in the vacuum zones. However, in the solid zones of the spacers,
513 only the faces' temperatures are defined, because the radiation effect only appears in the vacuum zones.
514 Further, the peripheral sides of the VIP are assumed to be adiabatic, owing to the symmetry of the
515 computational domain. Finally, thermally-coupled boundary conditions are used at all interfaces. In this
516 case, the temperature on the interfaces and the heat transfer rate are the same. The detailed mathematical
517 expressions of the boundary conditions are presented here for the frame-type spacer as an example.

518 At the hot wall:

519 For the spacer zones $T = T_h$; and

520 For the vacuum zones $T = T_h$ and $\varepsilon = \varepsilon_h$.

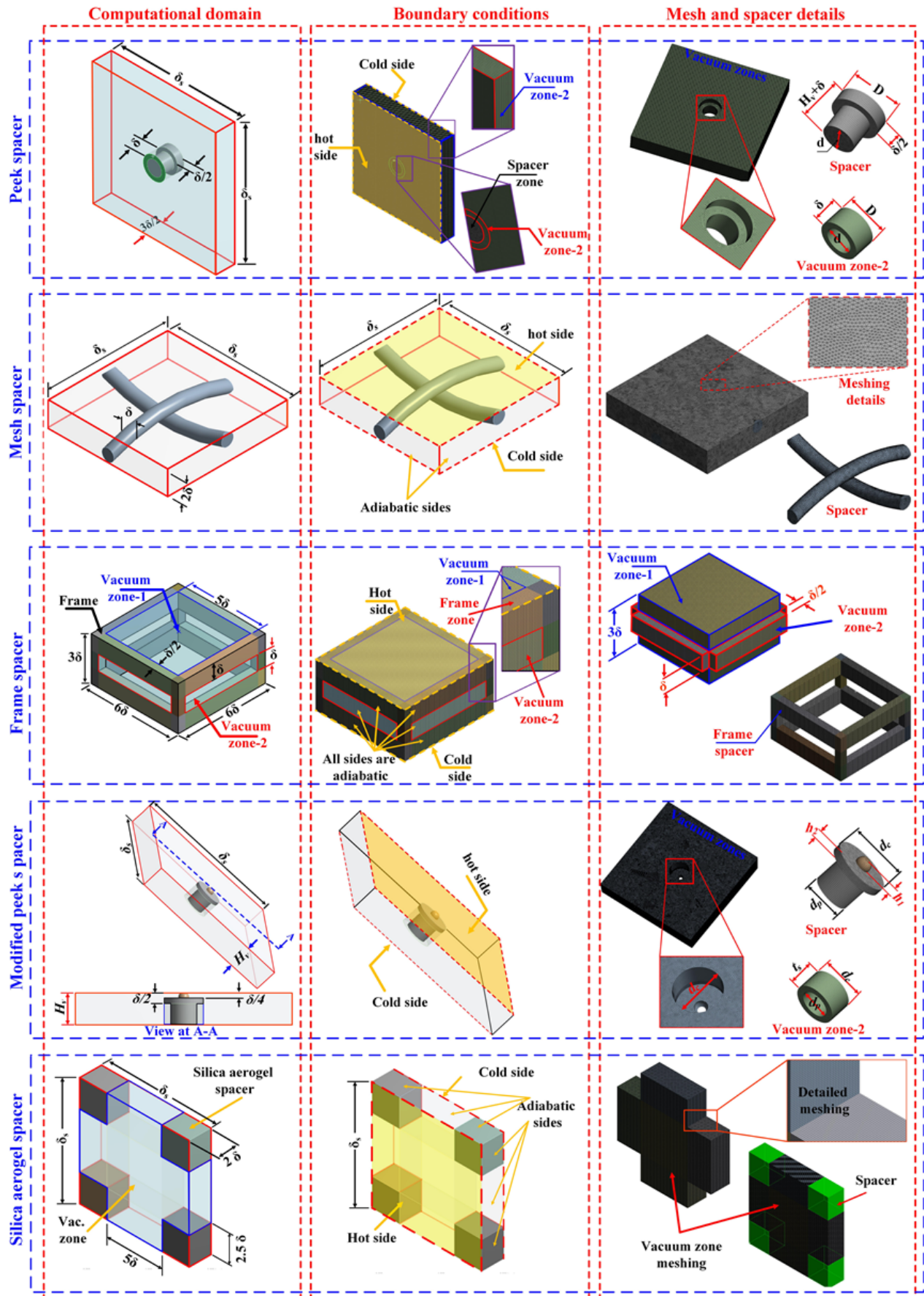
521 At the cold wall:

522 For the spacer zones $T = T_c$; and

523 For the vacuum zones $T = T_c$ and $\varepsilon = \varepsilon_c$.

524 A mesh independence test is performed to ensure that the results are independent on the number of elements.
525 After the test, a total of 1370521, 2450133, 1745551, 864000, and 1600000 elements are used for the
526 prediction of the centre-of-panel thermal conductivity of the peek spacer, modified peek spacer, mesh-type,
527 frame-type, and silica aerogel spacers, respectively.

528



529

530

Fig. 9 Computational domains, boundary conditions, and mesh details for all investigated cases.

531 **4.2. Numerical methods**

532 In the beginning, the computational domains presented in Fig. 9 are created using the "DesignModular"
533 tool, and using a multizone approach. In the multizone approach, the domain is divided into several zones
534 to enable control of the meshing, properties, and boundary conditions of each zone separately. In addition,
535 the interfaces between each zone and the neighbouring zones were thermally coupled. Then, the
536 computational domain is meshed. The mesh details for each core structure are displayed in Fig. 9 in the
537 right column. The model-governing equations are solved using the Fluent module. In Fluent, the energy
538 equation and fluid flow equations (including continuity and momentum) are standard equations, although
539 in this work, the vacuum zones are fluid. The very low pressure allows us to neglect the convection effect
540 and hence, the fluid flow equations can be eliminated (Fang et al., 2009, 2006; Memon et al., 2019b).
541 However, the S-S radiations model must include a fluid zone. Therefore, the vacuum layer is considered as
542 a fluid zone, but only the energy equation is enabled. The S-S radiation model estimates the orientation,
543 area, and spacing of each face participating in the radiation model. Therefore, the view factors can be
544 calculated. The energy equation for the solid layers and the energy equation for the vacuum space, including
545 the effects of S-S radiation, are simultaneously solved. Moreover, the radiosity evaluation is performed
546 based on the calculated view factors. To include the effects of pressure in the calculation, the vacuum region
547 thermal conductivity with the pressure is evaluated by using Equation (3) for each vacuum zone. Shell zone
548 conduction layers are added in the simulation to include the effects of the existing acrylic support plates. In
549 this case, the real thickness and the thermal conductivity of the acrylic plates must be added in the
550 simulation tool.

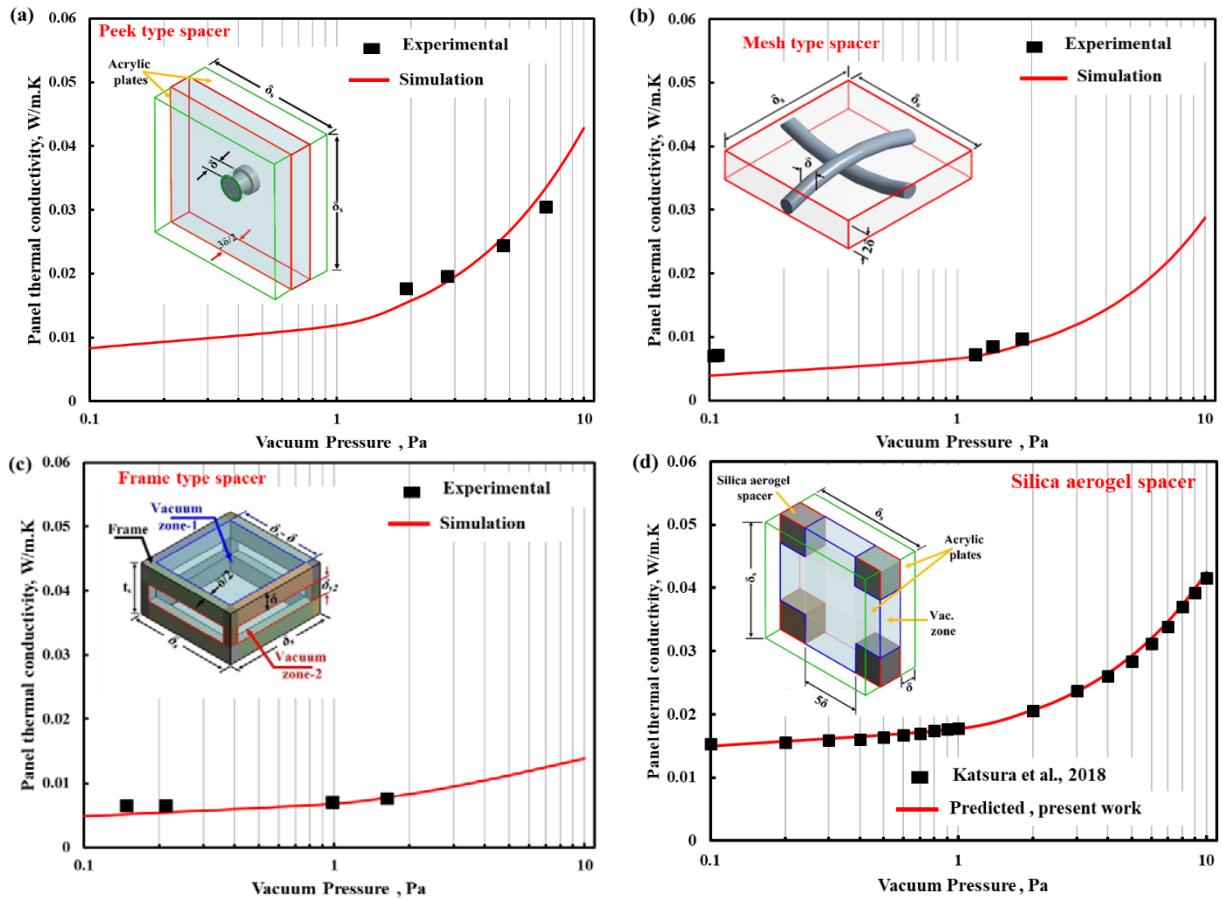
551

552 **4.3. Model validation**

553 The predicted centre-of-panel thermal conductivity is compared with the measured thermal conductivity
554 obtained by the Experiments in Section 3.2 for the peek type spacer, mesh-type spacer, and frame-type
555 spacer in Figs. 10-a, b, and c, respectively. Further, the currently-predicted results are compared with the
556 numerical results of (Katsura et al., 2018), as shown in Fig. 10-d. The model is examined under different
557 pressure values, from 0.1 to 10 Pa. Based on the comparisons depicted in Fig. 10-a, b, and c, it is observed
558 that the model accurately predicts the centre-of-panel thermal conductivity for the peek, mesh and frame-
559 type VIPs, with a maximum error of 11%. In addition, the error is higher at lower pressures, especially in
560 the mesh-type spacer. This may be attributed to two causes. First, at low pressure, the connections between
561 the rods become larger, owing to the flexibility of the rods. However, this is difficult to consider in the
562 calculation. This is also the reason that the predicted results are slightly lower than the experimental results,
563 especially in Fig 10-b. The second cause could be gas emissivity from the core structure.

564 In addition, the model is validated for the silica aerogel spacer studied in (Katsura et al., 2018). In this
565 part, the silica aerogel spacer dimensions, boundary conditions, and vacuum zone dimensions are the same
566 as those existing in (Katsura et al., 2018), and are displayed inside Fig. 10-d. The main difference between
567 the present model and the model developed by (Katsura et al., 2018) is that the current model is a 3D model
568 that uses S-S radiation, whereas the model developed in (Katsura et al., 2018) is one-dimensional. Based
569 on Fig. 10-d, an excellent agreement is observed. Although the current model nearly accomplishes the same

570 results as the one-dimensional model, the heat flux, and temperature contours can be obtained by the current
 571 model, and these parameters cannot be obtained using a one-dimensional model.

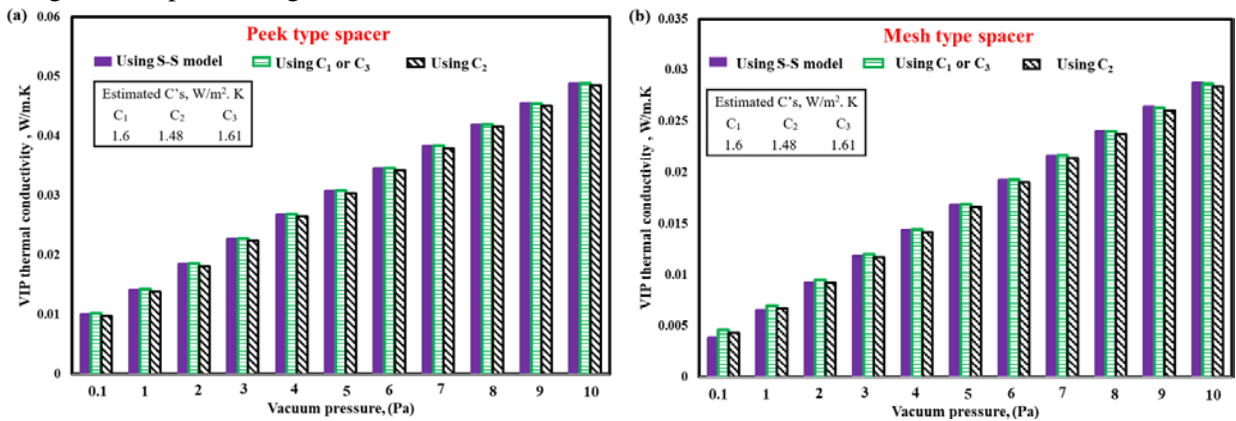


572 Fig. 10 Comparison of the predicted centre-of-panel thermal conductivities with (a) the experimental
 573 results for peek spacer; (b) the experimental results for mesh spacers; (c) experimental results of frame-
 574 type spacer; and (d) the numerical results of (Katsura et al., 2018).

575
 576 The S-S radiation model is compared with theoretical models using equivalent radiation conductance in
 577 the vacuum region, and the comparisons are presented in Figs. 11-a and b for the peek type and mesh-type
 578 VIPs as examples, respectively. It is evident that the S-S model accurately predicts the radiation exchange
 579 inside the VIP, as compared with the existing traditional methods using different correlations of C's. From
 580 Fig. 11-a, it can be seen that the predicted results using the S-S radiation model are very close to the results
 581 of using the models Equations (4), (8)m and (9). The estimated values of the radiation conductance using
 582 Equation (4) and Equation (9) are very close. Although the S-S radiation model considers the radiation
 583 exchange between all the surfaces in connection with the vacuum regions, the results of this model are very
 584 close to the results of using two surfaces' radiation exchanges, as proposed in Equations (4), (8), and (9) for
 585 pillar-supported VIPs. This is attributed to the fact that in VIPs, the vacuum space is very small, and the
 586 view factor between the spacer side and the radiant surfaces is also very small, owing to the smaller side
 587 area of the spacers. Therefore, the assumption of a unity view factor is a reasonable assumption, especially
 588 with smaller pillar- or peek-connection areas to the vacuum space. The maximum differences between the
 589 results of using the S-S model and other models using Equation (4) and Equation (8) are approximately
 590 1.6% and 3.4%, respectively, at the lower pressure level of 0.1 Pa for the peek-type spacer. However, by

591 increasing the pressure, the difference decreases. This is because the radiation contribution is higher at
 592 lower pressure, and increasing the pressure increases the gas conduction. At that time, the gas conduction
 593 becomes the dominant factor. This trend will be discussed in detail in the results section, by comparing the
 594 value of each heat transfer mode.

595
 596 In contrast, in the case of using a spacer with a larger surface area such as a mesh-type spacer (see Fig.
 597 11-b), the radiation exchange between the cold and hot surface could be affected by the view factor, owing
 598 to the existence of the spacer between these two walls. To confirm this, the predicted centre-of-panel
 599 thermal conductivity using the models in Equations (4), (8), and (9) is compared with the results predicted
 600 using the S-S model. It is evident that the relative differences between the results of S-S model and the
 601 results of Equations (4) and (8) are approximately 26% and 25.8%, respectively, at a pressure of 0.1 Pa.
 602 However, at higher pressures, where the gas conduction is dominant, the difference between these models
 603 decreases to approximately 2%. Therefore, based on the validation step and the model comparison, the use
 604 of the S-S model accurately predicts the radiation exchange inside the VIP, by an accurate estimation of the
 605 real view factor, based on the inner spacer design. In addition, the S-S model is very sensitive to every
 606 change in the spacer design.



607 Fig. 11 Comparison of the predicted centre-of-panel thermal conductivities using surface-to-surface (S-S)
 608 radiation model with the results of using the correlations for the equivalent conductance methods
 609 available in the literature for (a) peek spacer and (b) mesh-type spacer as examples.

610 5. Results and discussion

611 This section is divided into four subsections. Section 5.1 evaluates and presents the effects of spacer
 612 structure on the centre-of-panel thermal conductivity at different pressures. Section 5.2 compares
 613 experimental methods for trial production of the VIP. Section 5.3 analyses an experimental evaluation of
 614 VIP light transparency, along with a cost analysis. Finally, Section 5.4 provides 3D modelling of the
 615 investigated VIPs under American Society for Testing and Materials (ASTM) boundary conditions. In
 616 addition, the annual heat gain and heat loss in two different hot and cold regions in Japan are estimated
 617 while using the investigated VIPs, as attached to existing windows.

618

619 5.1. Centre-of-panel thermal conductivity estimation

620 In all of the simulated results, the emissivities of the hot and cold walls were measured using the setup

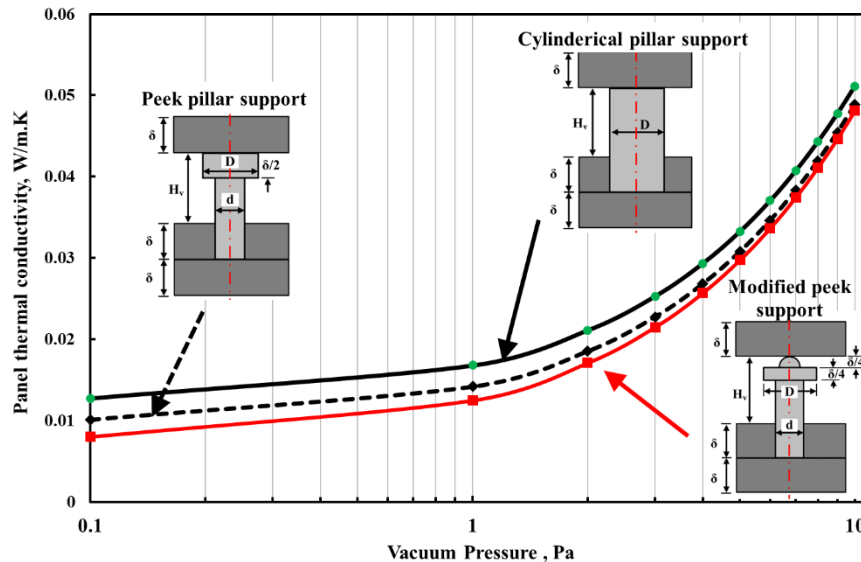
621 described in Section 3.1, and were found to be 0.28 and 0.9, respectively. The first emissivity is obtained
622 by using the L-e coated film. However, the second emissivity is the emissivity of the acrylic plates and the
623 core structures used in the experiments. In the simulation, all the faces coupled with the vacuum zones and
624 the hot and cold faces are considered to participate in the S-S radiation model. In addition, the steady-state
625 hot- and cold-side temperatures of the heat flow meter are kept constant at 35.5 °C and 10.5 °C, respectively.
626

627 The thermal conductivities of the polycarbonate spacers and acrylic plates are 0.2 W/m.K (Choi et al.,
628 2016). However, the vacuum zones' thermal conductivity changes according to the pressure levels. At the
629 low pressure of 0.1 Pa and a smaller thickness of the vacuum space of 2 mm, the vacuum region thermal
630 conductivity is estimated to be 2.1×10^{-4} W/m.K. This means that the spacer thermal conductivity is
631 approximately 950 times that of the vacuum region thermal conductivity. This ratio decreases to 9.5 times
632 at a pressure of 10 Pa. Therefore, it is expected that the conduction thermal bridge through the core structure
633 is a vital parameter that must be considered, especially at lower pressures. Hence, to decrease the heat
634 transfer rate through the core structure, a smaller connection is examined. This idea focuses on a reduction
635 in the conduction area, and consequently, a reduction in the thermal bridges through the spacer. To clarify
636 this point, a comparison is conducted for three cases of pillar-supported structures, and the results are
637 displayed in Fig. 12. In the first case, a regular cylindrical pillar with a diameter D of 1.8 mm is used to
638 obtain a vacuum gap with a thickness of 1.5 mm. In the second case, a peek-type pillar with a head diameter
639 D of 1.8 mm, thickness $\delta/2$ of 0.5 mm, and nail diameter d of 1.2 mm is used. In the final case, a modified
640 peek shape is theoretically proposed, by including a spherical head for the peek. To fix the pillars in these
641 three structures, two acrylic plates (1 mm each) are used in the simulation. Therefore, the total thickness of
642 the VIP in these three structures is 4.5 mm, as presented inside Fig 12. Fig. 12 presents the variation of the
643 VIP centre-of-panel thermal conductivity for these three cases with the pressure. It is evident that the new
644 modified peek attains a lower centre-of-panel thermal conductivity over the full range of the pressure, i.e.
645 from 0.1 Pa to 10 Pa. This because in the modified peek support, the connection between the hot and cold
646 walls is decreased by using the hemispherical head, in addition to reducing the support diameter from 1.8
647 mm to 1.2 mm.

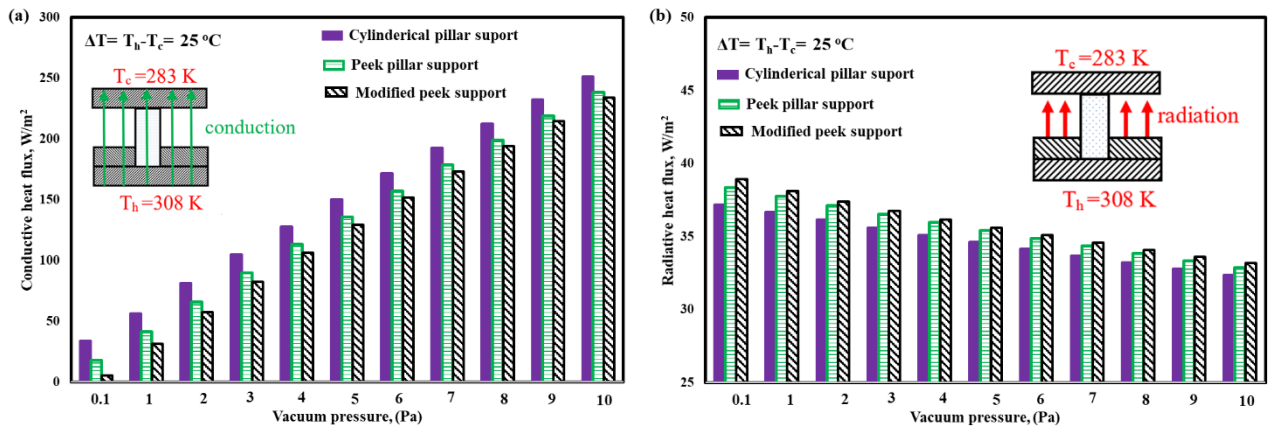
648 In more detail, the centre-of-panel thermal conductivity is reduced by approximately 37% and 5.9% at
649 pressures of 0.1 Pa and 10 Pa, respectively, with changing the conventional common cylindrical pillar to
650 the modified peek pillar. This reduction is attributed to the reduction in the conduction heat flux, as
651 presented in Fig. 13. In this figure, the variations of the conduction and radiation heat fluxes are displayed
652 for the pillar-supported designs at different pressures in Figs. 13-a and b, respectively. The area-weighted
653 average of the total heat transfer rate from the hot surface is estimated and divided by the total surface area
654 of the hot wall to obtain the total heat flux from the hot wall. After that, the area-weighted average of the
655 net radiation heat transfer rate from the hot wall is also calculated, and the radiation heat flux is estimated
656 by the dividing this value to the surface area of the hot wall. Finally, the conductive heat flux is estimated
657 by the subtraction of the radiation heat flux from the total heat flux. The predicted conduction heat flux
658 considers both the pillar conduction and the gas conduction in the vacuum space.
659

660 Based on Fig. 13-a, a significant reduction in the conduction heat flux is predicted while using the
 661 modified peek pillar support structure, especially at lower pressures. This may be attributed to two factors.
 662 The first is the reduction in the connection area between the hot and the cold walls. The second reason is
 663 that a very thin layer of low conductive vacuum exists between the top plate and the pillar circular head in
 664 the modified peek support, but does not exist in the cylindrical pillar support. This layer, with a thickness
 665 of $\delta/2$, has a very low thermal conductivity as compared with the pillar conductivity of 0.2 W/m.K.
 666 Therefore, a smaller conductive heat transfer could be attained. This reduction decreases with the pressure
 667 increase, because increasing the pressure increases the conduction through this very thin layer of the
 668 vacuum space. Consequently, it increases the VIP thermal conductivity. In more detail, at 0.1 Pa, changing
 669 the cylindrical pillar support to the modified peek support decreases the conduction heat flux from 35 W/m²
 670 to approximately 5.6 W/m².

671
 672 Meanwhile, the radiative heat flux is presented in Fig. 13-b. It is predicted that the radiative heat flux
 673 slightly decreases with an increase in pressure. This is attributed to the observation that at higher pressures,
 674 a higher conduction heat flux is obtained. This decreases the temperature differences between the inner
 675 surfaces in connection with the vacuum regions. Thus, a reduction in the radiative heat flux could be
 676 attained. This reduction is very small compared with the increase in the conduction heat flux. In more detail,
 677 with an increase in the pressure from 0.1 to 10 Pa, the conduction heat flux increases from 5.9 to 230 W/m²,
 678 whereas the radiation heat flux decreases from 38.6 W/m² to 33.5 W/m². In addition, the radiation heat flux
 679 in the case of using the modified peek support is higher than that when using the cylindrical support. This
 680 because of the increase in the vacuum region with the use of the modified peek support; the radiative heat
 681 flux increases from 37.1 to 38.9 W/m² when replacing the cylindrical pillar with the modified peek pillar
 682 at a pressure of 0.1 Pa.

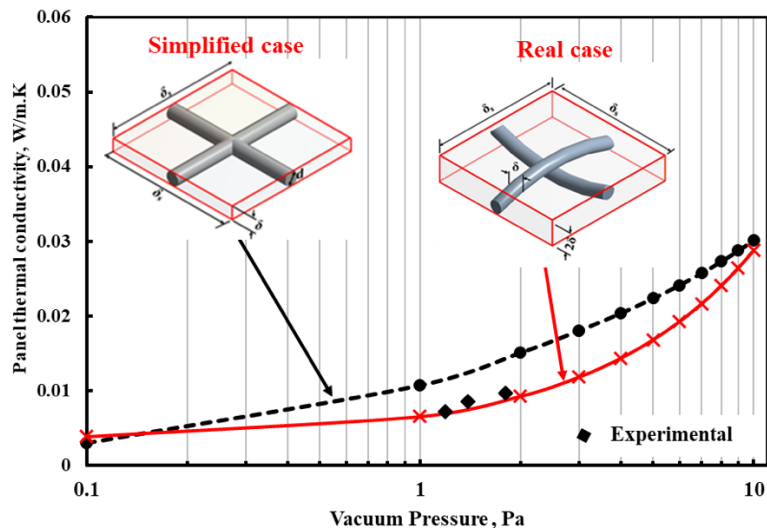


683
 684 Fig. 12 Variation of the predicted centre-of-panel thermal conductivity with the internal pressure for three
 685 different designs of pillar-supported VIPs.
 686



687 Fig. 13 Variation of (a) conductive heat flux and (b) radiative heat flux with the pressure levels for the
 688 three investigated pillar-supported structures.

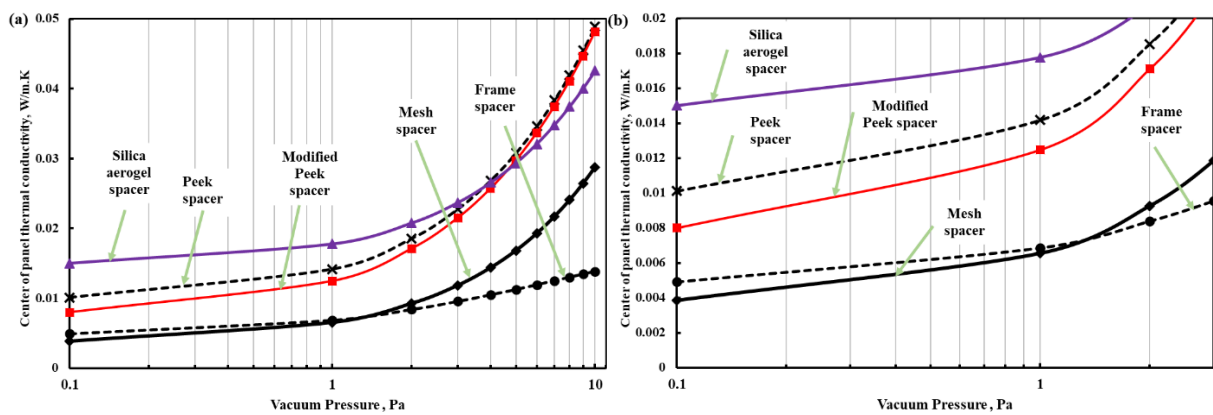
689
 690 At the beginning of the modelling, the mesh-type spacer is simplified and modelled as a round plus-
 691 shaped spacer, as seen in Fig. 14 (left side). The predicted centre-of-panel thermal conductivity, in this case,
 692 is compared with the experimental results. In this case, the computational fluid dynamic meshing is easier
 693 and faster than in an actual case. However, it is found the predicted results are higher than the experimental
 694 results. This because the connection between the spacer and the hot wall is larger than in the real case.
 695 Therefore, the real case for the mesh spacer is modelled, and the results are compared with the experiments.
 696 A good agreement is found, as discussed earlier in the validation step. Therefore, the actual mesh shape as
 697 presented in Fig. 14 (right side) is considered through the entirety of this work.



698
 699 Fig. 14 Comparison of the predicted centre-of-panel thermal conductivity with the experiments for the
 700 simplified and the real case of mesh spacer.

701
 702 Figure 15-a compares the variation of the centre-of-panel thermal conductivity for all investigated core
 703 structures at different pressure levels. From this figure, three findings can be determined. First, increasing
 704 the pressure increases the centre-of-panel thermal conductivity. Second, although the silica aerogel spacer
 705 has a lower thermal conductivity of 0.02 W/m.K, the silica aerogel VIP accomplished the highest centre-
 706 of-panel thermal conductivity among these structures at lower pressure levels. This because in the silica

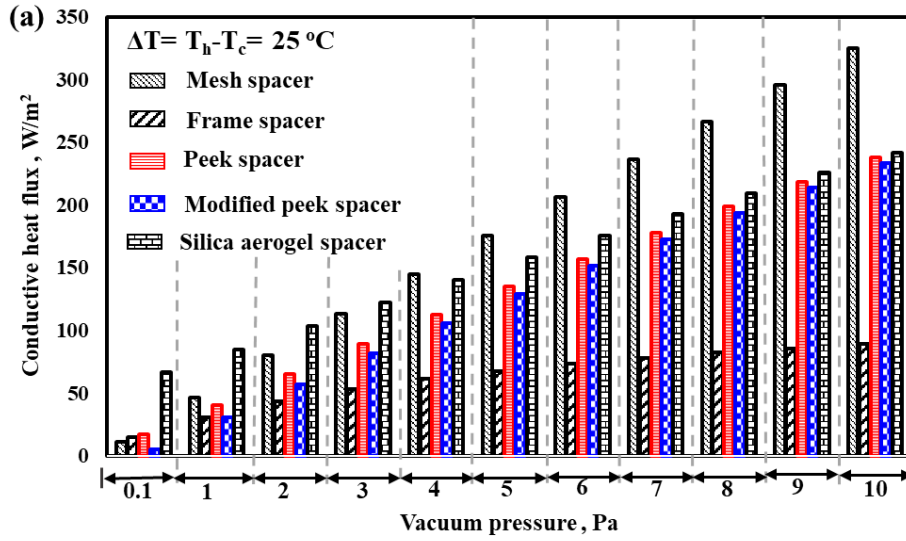
707 aerogel spacer, the ratio of the area occupied by the silica aerogel to the total area of the panel is
 708 approximately 25%, and the remaining 75% is occupied by vacuum. Therefore, this increase in silica
 709 aerogel area eliminates the benefit of its lower thermal conductivity as compared with other spacers.
 710 Therefore, a compromise between the heat transfer area and the spacer thermal conductivity is essential.
 711 However, the silica aerogel spacer cannot be easily manufactured in the form of other proposed structures,
 712 owing to its brittle structure with a low yield strength, which could lead to the VIP fracturing during the
 713 fabrication (Ma et al., 2018; Woignier et al., 2015). Finally, at low pressures below 1 Pa, the mesh-type and
 714 frame-type spacers attain the lowest panel thermal conductivity, at approximately 0.007 W/m.K. This is
 715 attributed to the reduction in thermal bridge attained in the spacer. In particular, in the mesh-type spacer,
 716 the connection area between the hot and cold side of the VIP is very small. For more clarification, Fig 15-
 717 b shows the variation of the centre-of-panel thermal conductivity with the pressure in a "zoomed in" smaller
 718 range, from 0.1 Pa to 3 Pa.



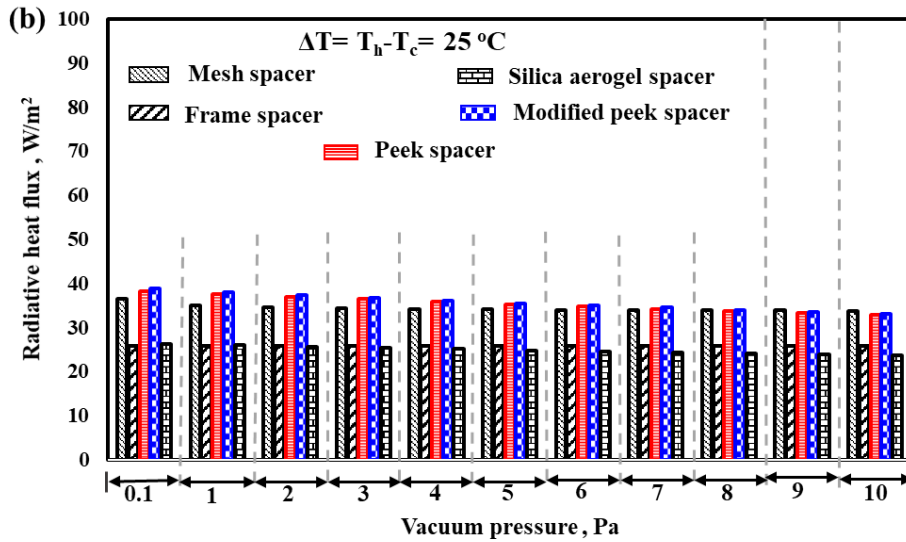
719
 720 Fig. 15 Variation of the predicted centre-of-panel thermal conductivity (a) for vacuum pressure from 0.1
 721 to 10 Pa and (b) for vacuum pressure from 0.1 to 3 Pa for all the structured-core transparent VIPs.
 722

723 Figs. 16-a and b show the variations of conductive heat flux and radiative heat flux attained in the studied
 724 VIPs, respectively. Generally, in Fig. 16-a, at pressures above 2 Pa, although the mesh spacer attains the
 725 highest conductive heat flux, it accomplishes the lowest VIP thermal conductivity. This because of the small
 726 thickness of this panel, at 2 mm. Similarly, at a pressure of 0.1 Pa, although the modified peek spacer has
 727 the lowest conductive heat flux, it does not attain the lowest VIP thermal conductivity. This is attributed to
 728 the fact that in pillar-supported VIPs, the total VIP thickness is much higher. This larger thickness increases
 729 the effective thermal conductivity. In more detail, in pillar-supported spacers, the total VIP thickness is 4.5
 730 mm, whereas for the mesh-type spacer, it is approximately 2 mm. This means that for the same total heat
 731 flux, the thermal conductivity of the pillar-supported VIP will be 2.25 times that of the mesh-type spacer.
 732 This is one of the main drawbacks of the pillar-supported VIPs mentioned in this work. The other drawback
 733 is that the manufacturing process is very difficult as compared with the other types of spacers, such as mesh-
 734 type spacers. From Fig. 16-b, it can be observed that the radiation heat flux decreases slightly for all
 735 investigated VIPs with an increase in pressure. Moreover, the frame-type and silica aerogel spacers obtained
 736 the lowest radiative heat flux. This is because in these spacers, the vacuum area in connection with the hot
 737 wall is at a minimum. This is also why the pillar-supported VIPs attain the maximum radiation heat flux,

738 i.e. the vacuum area in connection with the hot wall is at a maximum for pillar-supported VIPs.



739



740

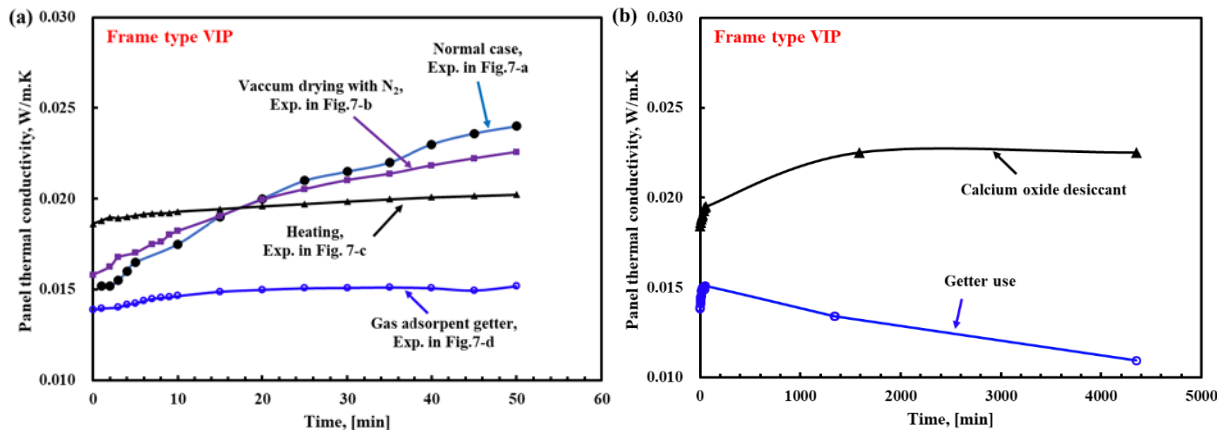
741 Fig. 16 Variations in (a) conductive heat flux and (b) radiative heat flux with pressure for the investigated
 742 VIPs.

743

744 **5.2. Trial production methods of VIP**

745 In Fig. 17-a, the predicted thermal conductivity variation with time is displayed for the four trial
 746 production methods explained in Section 3.3. The comparison is implemented for the frame-type VIP as an
 747 example. It is evident that using getter material during the manufacturing process of the VIPs accomplishes
 748 the lowest thermal conductivity in comparison with the use of other methods. In addition, the direct
 749 manufacturing of the VIP without the use of a calcium oxide adsorbent pack is the worst case. As the use
 750 of the getter accomplished the best results among these methods, a further trial method is implemented here
 751 to compare the predicted thermal conductivity of the frame-type VIP in the case of using two different types
 752 of outgassing adsorbent materials. The getter material is compared with the use of a calcium oxide desiccant
 753 inside a pack. The results are recorded for 75 h, and are displayed in Fig. 17-b. It is noticeable that the use
 754 of getter material accomplished the lowest panel effective thermal conductivity in comparison with the use

755 of calcium oxide desiccant packs. The lowest thermal conductivity attained in the case of using getter was
 756 approximately 0.011 W/m.K, which is equivalent to 5 Pa. This means that the inside pressure increased
 757 after the sealing, owing to the gas emissivity. The effect of this parameter will be investigated in the authors'
 758 future work.



759
 760 Fig. 17 variation of the centre-of-panel thermal conductivity with the elapsed time for (a) different trial
 761 manufacturing methods and (b) different two outgassing adsorbent materials.
 762

763 5.3. Light transparency and cost analysis

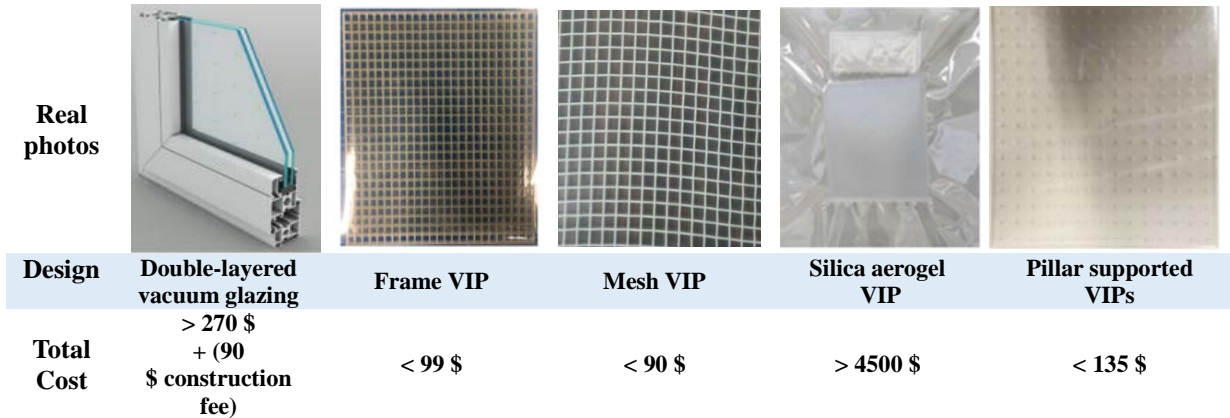
764 This section presents the transparency measurements of the proposed VIPs, and the cost analysis. Table
 765 3 displays the measured transparency of the manufactured VIPs with different core structures. In this
 766 experiment, the illuminance is measured with and without VIP shading. The ratio displayed in the table
 767 represents the measured light intensity in a case with the VIP to a reference case where no VIP exists. Here,
 768 it is worth mentioning that the measured transparency is only for the VIPs without the single-layered glass
 769 window of 3 mm. It is evident that the transparency of the manufactured VIPs ranges from 0.65 to 0.9, for
 770 the mesh-type spacer to the cylindrical-pillar spacer, respectively. In addition, as the modified peek spacer
 771 is only numerically investigated, the expected transparency could be similar to that of the peek type spacer.
 772

773 Table 3. Measured transparency for the experimentally-examined VIPs

Conditions	Without VIP	Silica aerogel spacer	Peek type spacer	Mesh-type spacer	Frame-type spacer
Intensity ($\mu W/cm^2/nm$)	20000	14000	17500	13000	15000
Transparency Ratio	1	0.70	0.88	0.65	0.75

774
 775 The cost of the proposed VIPs is compared with the most common insulating method, which uses vacuum
 776 double-glazing insulation technology. The comparison is made for a 1 m² window, and is presented in Fig.
 777 18. Further, the cost of the VIPs includes the cost of all of the used materials, including the envelope,
 778 spacers, and L-e coating films, as presented in detail in Table 4. Based on the available data, it is evident
 779 that the insulation cost of using VIPs represents approximately one-third of the cost of an insulation method
 780 using double-glazing. In addition, the idea proposed in this work can be effectively applied to the windows

781 of existing buildings by attachment or by using it as a curtain, with a very low cost as compared to the use
 782 of silica aerogel VIPs. Finally, based on Table 4, it is evident that the L-e film represents approximately
 783 half the price of the VIP.



784 Fig. 18. Comparison of the calculated production cost of proposed VIPs with the double-layered vacuum
 785 glazing insulation.

786 Table 4 Detailed costs of the manufactured VIPs (\$ /m²)

Item	Mesh spacer	Frame spacer	Peek spacer	Silica aerogel
Core material	9 \$	18 \$	36 \$ (plates + pillars)	4401 \$
L-e film	45 \$	45 \$	45 \$	45 \$
Envelope	18 \$	18 \$	18 \$	18 \$
Manufacturing fee + adsorbent	18 \$	18 \$	36 \$	36 \$
Total cost	90 \$	99 \$	135 \$	4500

787
 788 **5.4. Energy analysis**
 789 This section evaluates the thermal performance when attaching the proposed VIPs to a 3 mm single-
 790 layered glass window, based on the ASTM standards (Section 5.4.1), and based on real meteorological
 791 conditions (Section 5.4.2).

792
 793 **5.4.1. Thermal performance analysis under American Society for Testing and Materials (ASTM)**
 794 **boundary conditions**

795 In this section, the developed 3D model is solved for the proposed VIPs when attached to a conventional
 796 glass window with a 3 mm thickness. The aim of this section is to estimate the temperature contours, heat
 797 flux transfer, and U-value of the system. The schematic of the modelled system consists of a 3 mm glass
 798 layer attached to the VIPs, as shown in Fig. 19. The boundary conditions are used as recommended by the
 799 ASTM standards for winter conditions, and as used by (Fang et al., 2009). In these boundary conditions,
 800 the indoor and outdoor ambient air temperatures were assumed constant at 21.1 and -17.8 °C, respectively.
 801 In addition, the convective heat transfer coefficients on the inside and the outside surfaces of the VIP with
 802 the glass window were set to be 8.3 and 30 W/m².K, respectively.

803
 804 The predicted 3D isotherms on the vacuum space at a vacuum pressure of 0.1 Pa are presented in Fig.
 805 19. Fig. 19 shows that a substantial temperature difference prevails between the two sides of the vacuum

806 layer. The highest temperature difference is accomplished for the mesh-type spacer. In addition, the use of
 807 a mesh-type VIP attached to the existing window with 3 mm single-layered glass thickness decreases the
 808 U-value from 6.3 to 1.14 W/m².K. This substantial reduction in the U-value decreases the heat loss from
 809 the building. In addition, by using the silica aerogel spacer, a higher U-value is obtained. This because high
 810 heat is transferred through the silica aerogel spacer, as previously explained and predicted using the
 811 temperature contours.

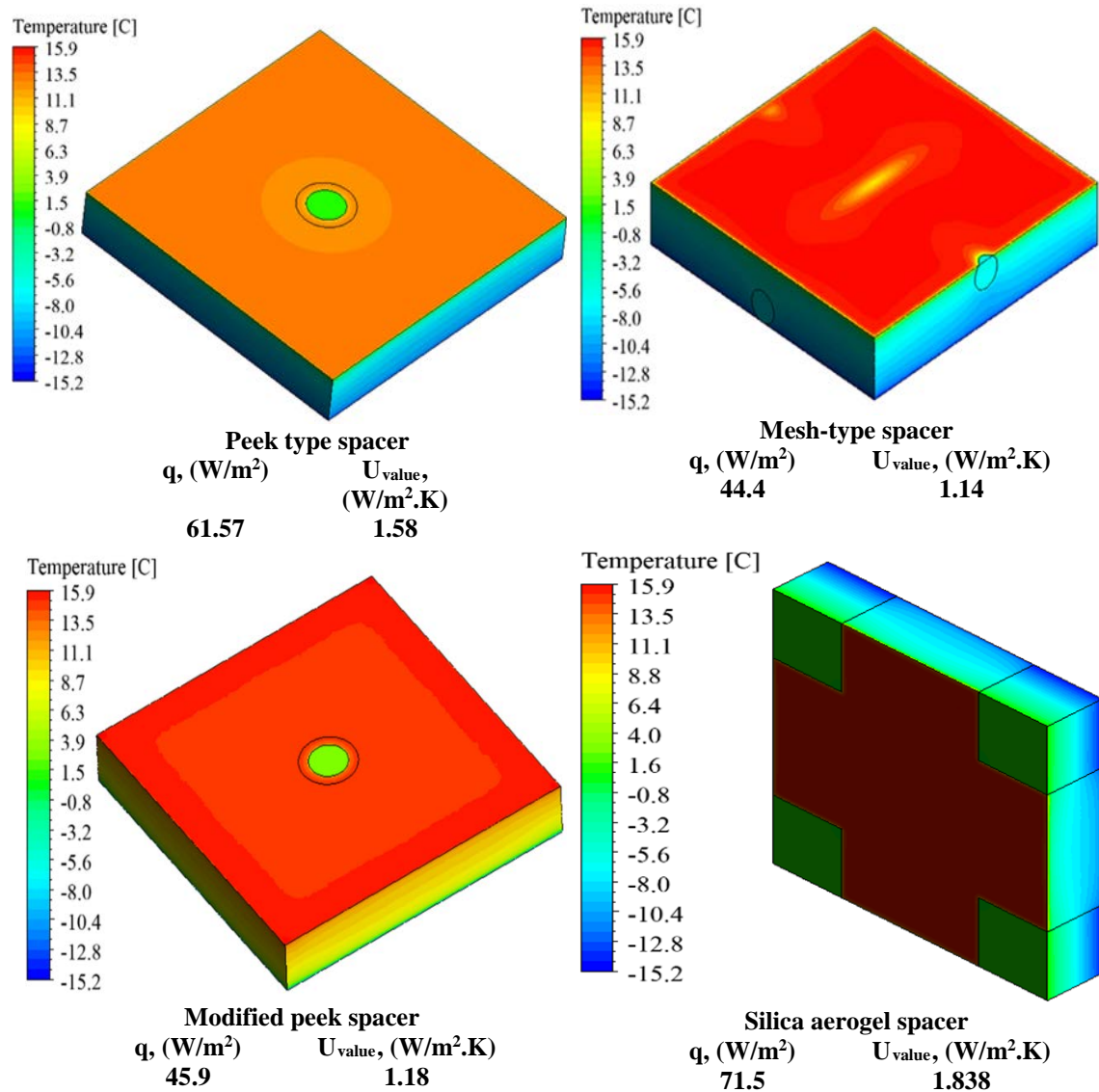


Fig. 19 Predicted 3D temperature contours of the investigated VIPs using American Society for Testing and Materials (ASTM) boundary conditions.

812
 813 **5.4.2. Annual energy analysis**
 814 This section is used to estimate the hourly and total annual thermal energy transferred through the
 815 proposed VIP when attached to the 1 m² single-layered glass window with 3 mm thickness. Moreover, the
 816 total rates of thermal energy transferred with and without the use of VIPs are compared. In this calculation,
 817 the inner air temperature is assumed to be at 20 °C, with an inside convective heat transfer coefficient of
 818 7.7 W/m².K (Fang et al., 2010; Memon et al., 2019b). In addition, the calculation uses the actual ambient
 819 temperatures and wind speed in Japan, by examining Ishigaki island (24.41° N, 124.17° E) as a hot region,

820 and Sapporo, Hokkaido (43.06° N, 141.35° E) as a cold region. The hourly ambient temperature and wind
821 speed are presented in Figs. 20-a and b, respectively. These meteorological conditions are measured by the
822 authors for Ishigaki, and are downloaded from Japan Meteorological Agency website for Sapporo. In-house
823 MATLAB code is developed to estimate the hourly and the annual thermal energy transfer. The model
824 adopted in this section is a one-dimensional quasi-steady model. This model is an efficient for a long-term
825 energy evaluation, as it predicts results with reasonably accepted accuracy in a short period of time. In this
826 model, the contact thermal resistance effect between the VIP and the glass window is not considered in the
827 calculation. In addition, it is also assumed that no solar radiation strikes the exterior surface of the window.
828 Therefore, the sol-air effect is neglected. The steady-state conduction heat flux transfer from the outside to
829 the interior of the building through the VIP-glass window system is calculated as follows:

$$830 \quad q = \frac{(T_a(t) - T_i)}{\left(\frac{1}{h_{c,i}} + \frac{\delta_g}{k_g} + \frac{\delta_v}{k_v} + \frac{1}{h_{c,o}(t)}\right)} \quad (22)$$

831 In the above, q , δ_g , k_g , δ_v , k_v , and $h_{c,i}$ are the rate of total thermal heat flux transfer in W/m², glass thickness
832 in m, glass thermal conductivity in W/m.K, VIP thickness in m, VIP thermal conductivity in W/m.K, and
833 the inside convective heat transfer coefficient in W/m².K, respectively. A negative value of q denotes a heat
834 loss from the building, which occurs when the outside temperature is less than the inside designed
835 temperature. Instead of using a constant for the outside convective heat transfer coefficient during the
836 simulation, it is taken from the wind speed and ambient temperature-dependent equation derived by
837 Nusselt-Jürges, and described in detail in (Palyvos, 2008). This equation is written for smooth surfaces,
838 such as the exterior surfaces of windows, as follows (Palyvos, 2008):

$$839 \quad h_{c,o}(t) = 5.678 \left\{ 0.99 + 0.21 \times \left[\left(\frac{294.26}{273.16 + T_a(t)} \right) \times \frac{U_\infty(t)}{0.3048} \right] \right\} \quad \text{at } U_\infty(t) < 4.88 \left(\frac{m}{s} \right)$$

$$840 \quad h_{c,o}(t) = 5.678 \left\{ 0.5 \times \left[\left(\frac{294.26}{273.16 + T_a(t)} \right) \times \frac{U_\infty(t)}{0.3048} \right]^{0.78} \right\} \quad \text{at } 4.88 \leq U_\infty(t) < 30.48 \left(\frac{m}{s} \right) \quad (23)$$

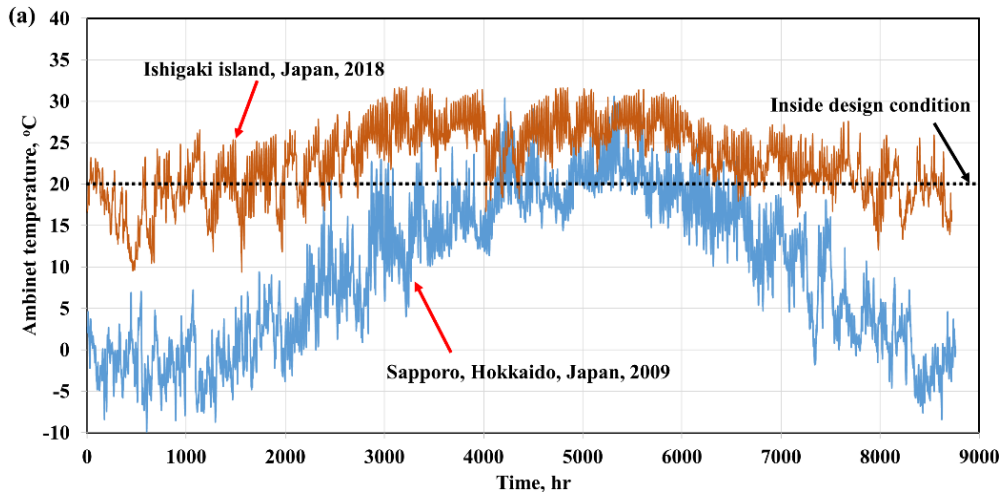
841 Here, $h_{c,o}(t)$, $T_a(t)$, and $U_\infty(t)$ are the hourly convective heat transfer coefficient from the exterior
842 surfaces of the window in W/m².K, the ambient temperature variation with the time in °C, and the wind
843 speed in m/s, respectively. The constants in Equation (23) are empirical constants derived from the
844 experiments developed by Nusselt-Jürges. Table 5 shows the thicknesses of the VIPs with the relevant
845 thermal conductivities at a pressure of 1 Pa.

846 Table 5 Detailed thickness and centre-of-panel thermal conductivities of the investigated VIPs at 1 Pa

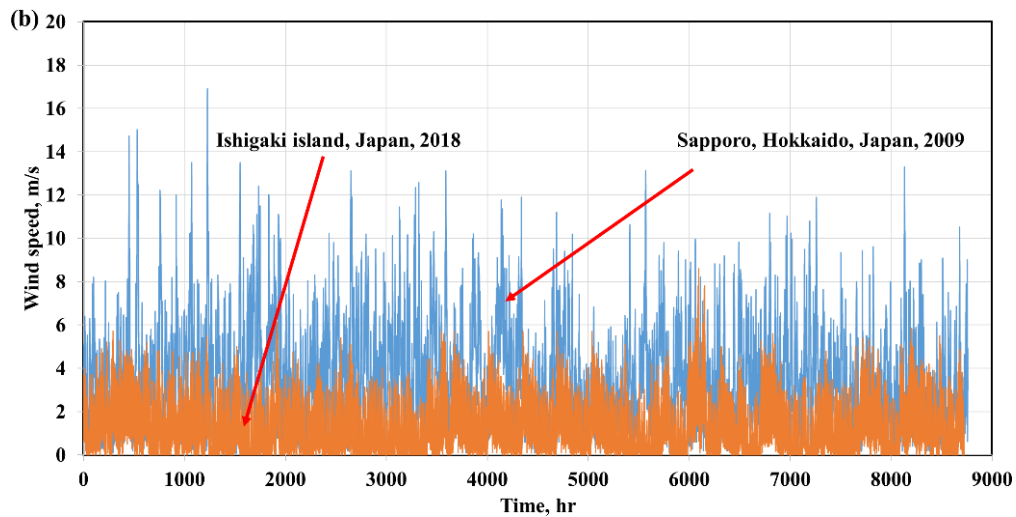
	Peek spacer	Mesh spacer	Cylindrical pillar	Frame spacer	Modified peek spacer	Silica aerogel
Thickness, (mm)	4.5	2	4.5	3	4.5	4
k_v @ 1 Pa, (mW/m.K)	14.2	6.5	16.7	6.8	12.4	17.7

847 The hourly variation of the thermal heat flux transfer in W/m², for both the single-layered glass window
848 and the proposed system of using a glass window with frame-type VIP as an example, is displayed in Figs.
849 21-a and b for Sapporo and Ishigaki, respectively. Based on these two figures, it is evident that attaching
850 the VIP to the single-layer glass windows of existing buildings reduces the heat loss from the building and
the heat gains to the buildings in cold and hot weather conditions, respectively. Further, it is highly

851 recommended to apply this idea in cold regions such as Sapporo, as the high temperature difference between
852 the outside ambient temperature and the inside designed conditions can be very high some days, e.g.
853 reaching 30 °C.



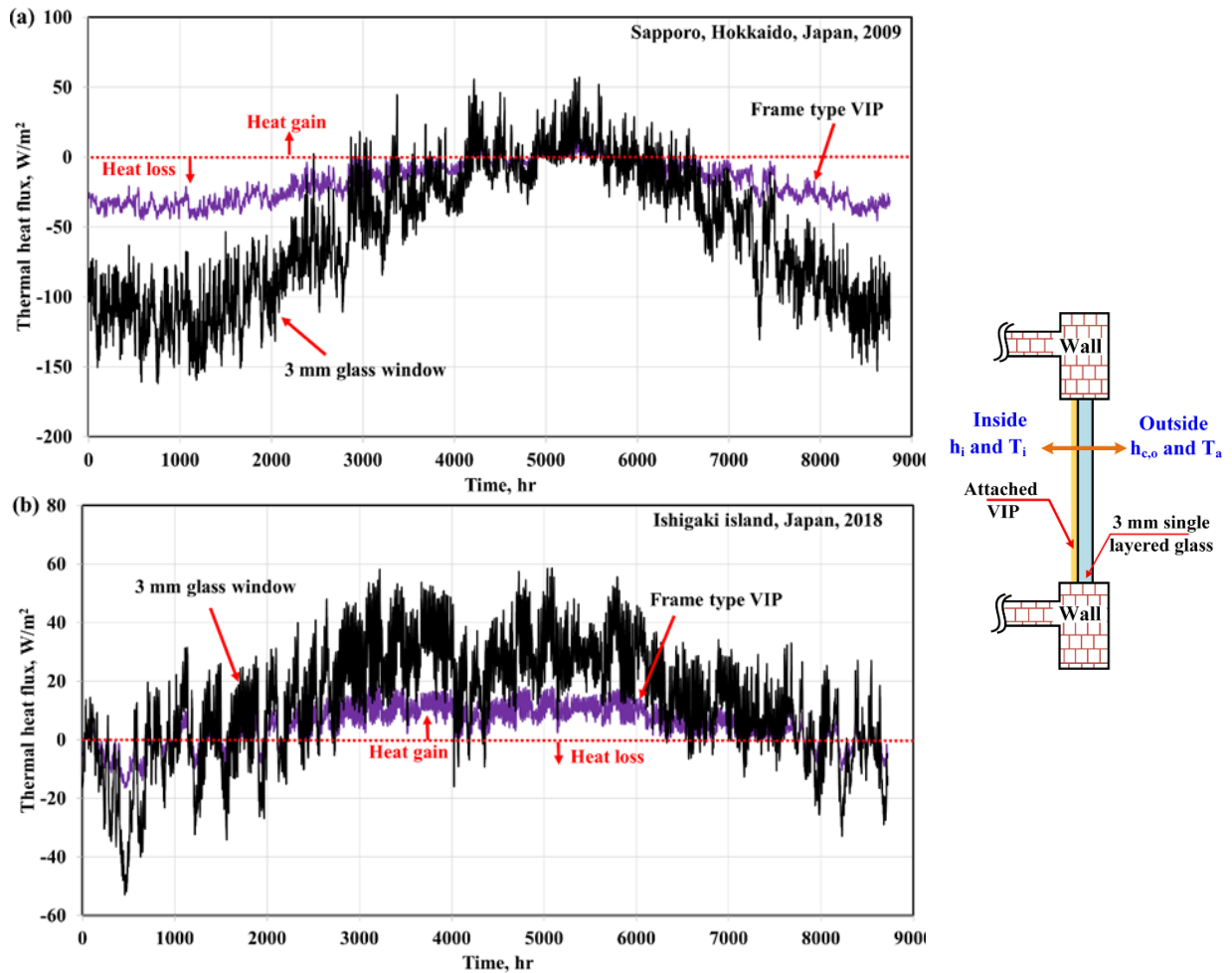
854



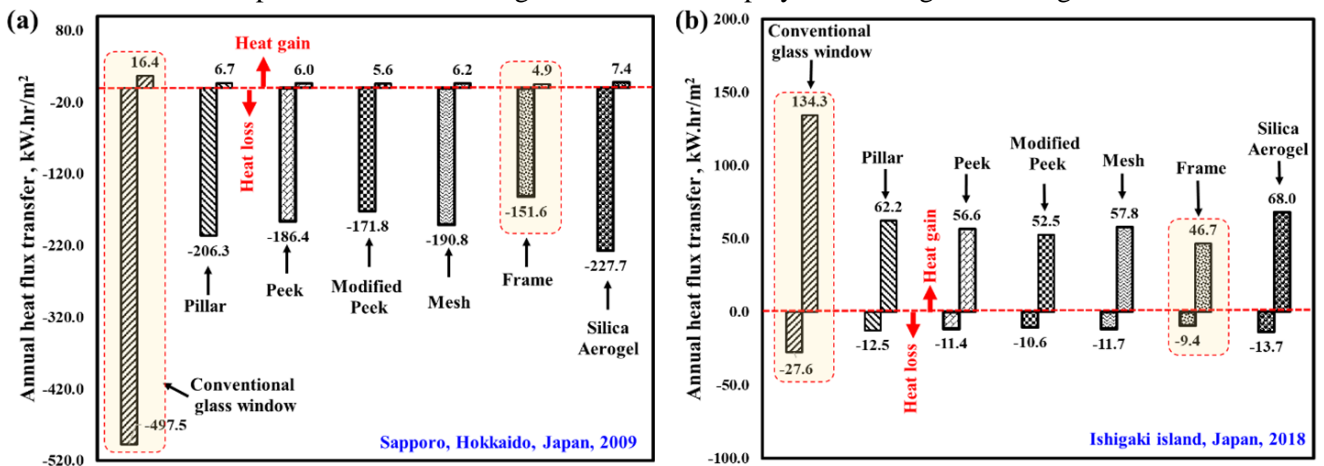
855

856 Fig. 20 Hourly variation of (a) ambient temperature and (b) wind speed for Ishigaki and Sapporo cities in
857 Japan.

858 The total annual thermal energy flux transfer in kW.h/m² is calculated and compared for all of the studied
859 VIPs in Figs. 22-a and b for Sapporo and Ishigaki, respectively. First, the total annual rate heat flux transfer
860 in W/m² is divided into loss and gain. The hourly integrations of both rates are displayed in the figure. For
861 the Sapporo region, it is evident that the total annual heat flux loss is much higher than the heat gain in this
862 region, owing to the cold weather. In addition, using a frame VIP attached to 3 mm glass window reduces
863 the heat loss from the buildings by up to 69.5%. In contrast, for Ishigaki region, the heat gain from the
864 window is much higher than the heat loss, and a 65.1% reduction in the annual heat gain is accomplished
865 by attaching the frame-type VIP to the existing 3 mm glass windows.



866 Fig. 21 Hourly variation of the thermal heat flux transfer in W/m^2 for (a) Sapporo and (b) Ishigaki in the
 867 case of using single-layered glass window and the frame-type VIP attached to the glass window as an
 868 example. The VIP with the glass window is displayed at the right of the figure.



869 Fig. 22 Variation of the total annual heat flux transfer in a unit of $kW.h/m^2$ for (a) Sapporo and (b)
 870 Ishigaki region.

871
 872
 873

874

875 **6. Conclusions**

876 The present study proposes five new and distinct structured-core transparent VIPs. These VIPs are
877 different from the well-known conventional VIP, which has a solid core material structure and opaque
878 metallized film barrier envelope. The VIPs herein are proposed so as to accomplish high thermal insulation
879 for the windows of existing buildings. The centre-of-panel thermal conductivity, transparency, and cost are
880 experimentally evaluated. In addition, four trial manufacturing methods for these VIPs are proposed and
881 compared. Further, a 3D thermal model is developed and numerically solved, and is validated via
882 experiments. Based on the results, it is determined that the frame and mesh-type spacers accomplished the
883 lowest centre-of-panel thermal conductivities of 6.5×10^{-3} and 6.8×10^{-3} W/m.K at a vacuum pressure of 1
884 Pa with thicknesses of 3 mm and 2 mm, respectively. Further, it is concluded that the use of a getter
885 adsorbent material during the manufacturing process of the VIPs keeps the inside pressure stable for a
886 longer period of time. Furthermore, at ASTM boundary conditions, the predicted U-values for the mesh
887 spacers and conventional silica aerogel spacers were 1.14 W/m².K and 1.84 W/m².K, respectively. However,
888 the use of mesh spacers is economically competitive with silica aerogels.

889

890 **Acknowledgements**

891 This work is financially supported by the Grants-in-Aid for Scientific Research of the JSPS (Research
892 representative: Takao Katsura). The authors also thank Mr. Masahiro Aihara, Ms. Ririko Noda in
893 Graduate School of Hokkaido University, Mr Yuji Mori in Faculty of Engineering, Hokkaido University,
894 Hokkaido Electric Power Co. Inc., Mitsubishi Chemical Corporation, Teijin Frontier Co., Ltd., ULVAC Inc.,
895 and Miyoshi Vacuum Packing for their assistance in the VIP test production.

896 **Nomenclature**

897 *A* vacuum insulation panel front area [m²]
898 *C* thermal conductance [W/(m².K)]
899 *C_b* black body radiation constant factor [W/(m².K⁴)]
900 *E* emissive power density [W/m²]
901 *F* radiation view factor [unitless]
902 *h_{c,i}* convective heat transfer coefficient inside the building [W/(m².K)]
903 *h_{c,o}* convective heat transfer coefficient on the outer glass surface [W/(m².K)]
904 *J* radiosity [W/m²]
905 *k* thermal conductivity [W/(m.K)]
906 *l_v* VIP thickness [m]
907 *P* pressure [N/m²]
908 *q* heat flux either on the hot or the cold side of the VIP [W/m²]
909 *T* temperature [°C]
910 *U_∞* wind speed [m/s]

911 **Greek symbols**

912 *Δ* difference

913	δ	thickness [m]
914	ε	emissivity [unitless]
915	λ_o	thermal conductivity of the air at the room temperature and pressure [W/(m.K)]
916	λ_v	thermal conductivity of the vacuum space [W/(m.K)]
917	σ	Stephan Boltzmann constant 5.67×10^{-8} [W/(m ² .K ⁴)]

918 **Subscripts**

919	a	ambient
920	avg	average
921	c	cold side of the VIP
922	eff	effective
923	g	glass
924	h	hot side of the VIP
925	$h-c$	between the hot and the cold side of the VIP
926	i	inside the building
927	in	entering the surface
928	out	exiting from the surface
929	v	VIP

930

931 **References**

- 932 ANSYS FLUENT Theory Guide, 2011.
- 933 Araki, K., Kamoto, D., Matsuoka, S. ichi, 2009. Optimization about multilayer laminated film and getter
 934 device materials of vacuum insulation panel for using at high temperature. J. Mater. Process. Technol.
 935 209, 271–282. <https://doi.org/10.1016/j.jmatprotec.2008.01.054>
- 936 Arya, Farid, Moss, R., Hyde, T., Shire, S., Henshall, P., Eames, P., 2018. Vacuum enclosures for solar
 937 thermal panels Part 1: Fabrication and hot-box testing. Sol. Energy 174, 1212–1223.
 938 <https://doi.org/https://doi.org/10.1016/j.solener.2018.10.064>
- 939 Arya, F., Moss, R., Hyde, T., Shire, S., Henshall, P., Eames, P., 2018. Vacuum enclosures for solar thermal
 940 panels Part 2: Fabrication and hot-box testing. Sol. Energy 1212–1223.
 941 <https://doi.org/10.1016/j.solener.2018.10.064>
- 942 Baetens, R., Jelle, B.P., Thue, J.V., Tenpierik, M.J., Grynning, S., Uvsløkk, S., Gustavsen, A., 2010. Vacuum
 943 insulation panels for building applications: A review and beyond. Energy Build. 42, 147–172.
 944 <https://doi.org/10.1016/j.enbuild.2009.09.005>
- 945 Boafu, F.E., Kim, J.-H., Kim, J.-T., 2019. Numerical study of slim curtain wall spandrel with integrated
 946 vacuum insulation panel: Concept, performance evaluation and challenges. Energy Build. 183, 139–
 947 150. <https://doi.org/https://doi.org/10.1016/j.enbuild.2018.10.036>
- 948 Bouquerel, M., Duforestel, T., Baillis, D., Rusaouen, G., 2012a. Heat transfer modeling in vacuum
 949 insulation panels containing nanoporous silicas - A review. Energy Build. 54, 320–336.
 950 <https://doi.org/10.1016/j.enbuild.2012.07.034>
- 951 Bouquerel, M., Duforestel, T., Baillis, D., Rusaouen, G., 2012b. Mass transfer modeling in gas barrier

952 envelopes for vacuum insulation panels: A review. *Energy Build.* 55, 903–920.
953 <https://doi.org/10.1016/j.enbuild.2012.09.004>

954 Buratti, C., Moretti, E., Zinzi, M., 2017. High Energy-Efficient Windows with Silica Aerogel for Building
955 Refurbishment: Experimental Characterization and Preliminary Simulations in Different Climate
956 Conditions. *Build.* . <https://doi.org/10.3390/buildings7010008>

957 Choi, B., Yeo, I., Lee, J., Kang, W.K., Song, T.H., 2016. Pillar-supported vacuum insulation panel with
958 multi-layered filler material. *Int. J. Heat Mass Transf.* 102, 902–910.
959 <https://doi.org/10.1016/j.ijheatmasstransfer.2016.06.032>

960 Collins, R.E., Simko, T.M., 1998. Current status of the science and technology of vacuum glazing. *Sol.*
961 *Energy* 62, 189–213. [https://doi.org/10.1016/S0038-092X\(98\)00007-3](https://doi.org/10.1016/S0038-092X(98)00007-3)

962 Fang, Y., Eames, P.C., Norton, B., Hyde, T.J., 2006. Experimental validation of a numerical model for heat
963 transfer in vacuum glazing. *Sol. Energy* 80, 564–577.
964 <https://doi.org/https://doi.org/10.1016/j.solener.2005.04.002>

965 Fang, Y., Eames, P.C., Norton, B., Hyde, T.J., Zhao, J., Wang, J., Huang, Y., 2007. Low emittance coatings
966 and the thermal performance of vacuum glazing. *Sol. Energy* 81, 8–12.
967 <https://doi.org/10.1016/j.solener.2006.06.011>

968 Fang, Y., Hyde, T., Hewitt, N., Eames, P.C., Norton, B., 2009. Comparison of vacuum glazing thermal
969 performance predicted using two- and three-dimensional models and their experimental validation.
970 *Sol. Energy Mater. Sol. Cells* 93, 1492–1498.
971 <https://doi.org/https://doi.org/10.1016/j.solmat.2009.03.025>

972 Fang, Y., Hyde, T.J., Hewitt, N., 2010. Predicted thermal performance of triple vacuum glazing. *Sol. Energy*
973 84, 2132–2139. <https://doi.org/https://doi.org/10.1016/j.solener.2010.09.002>

974 Fantucci, S., Garbaccio, S., Lorenzati, A., Perino, M., 2019. Thermo-economic analysis of building energy
975 retrofits using VIP - Vacuum Insulation Panels. *Energy Build.* 196, 269–279.
976 <https://doi.org/https://doi.org/10.1016/j.enbuild.2019.05.019>

977 Fricke, J., Heinemann, U., Ebert, H.P., 2008. Vacuum insulation panels-From research to market. *Vacuum*
978 82, 680–690. <https://doi.org/10.1016/j.vacuum.2007.10.014>

979 Incropera, F.P., DeWitt, D.P., Bergman, T.L., Lavine, A.S., 2007. *Fundamentals of Heat and Mass Transfer,*
980 *Water, Dekker Mechanical Engineering. John Wiley & Sons.*
981 <https://doi.org/10.1016/j.applthermaleng.2011.03.022>

982 Jang, C., Kim, J., Song, T.H., 2011. Combined heat transfer of radiation and conduction in stacked radiation
983 shields for vacuum insulation panels. *Energy Build.* 43, 3343–3352.
984 <https://doi.org/10.1016/j.enbuild.2011.08.036>

985 Johansson, P., Adl-Zarrabi, B., Hagentoft, C.E., 2012. Using transient plane source sensor for determination
986 of thermal properties of vacuum insulation panels. *Front. Archit. Res.* 1, 334–340.
987 <https://doi.org/10.1016/j.foar.2012.09.004>

988 Jung, H., Yeo, I., Song, T.H., 2014. Al-foil-bonded enveloping and double enveloping for application to
989 vacuum insulation panels. *Energy Build.* 84, 595–606. <https://doi.org/10.1016/j.enbuild.2014.08.045>

990 Katsura, T., Yang, Z., Aihara, M., Nakamura, M., Nagano, K., 2018. Development of Slim and Translucent

991 Vacuum Insulation Panels. *J. Japan Sol. Energy Soc.* 44, 49–57. https://doi.org/10.24632/jses.44.2_49

992 Kim, J., Jang, C., Song, T.H., 2012a. Combined heat transfer in multi-layered radiation shields for vacuum
 993 insulation panels: Theoretical/numerical analyses and experiment. *Appl. Energy* 94, 295–302.
 994 <https://doi.org/10.1016/j.apenergy.2012.01.072>

995 Kim, J., Lee, J.H., Song, T.H., 2012b. Vacuum insulation properties of phenolic foam. *Int. J. Heat Mass*
 996 *Transf.* 55, 5343–5349. <https://doi.org/10.1016/j.ijheatmasstransfer.2012.05.051>

997 Kim, J., Song, T.H., 2013. Vacuum insulation properties of glass wool and opacified fumed silica under
 998 variable pressing load and vacuum level. *Int. J. Heat Mass Transf.* 64, 783–791.
 999 <https://doi.org/10.1016/j.ijheatmasstransfer.2013.05.012>

1000 Kwon, J.S., Jang, C.H., Jung, H., Song, T.H., 2010. Vacuum maintenance in vacuum insulation panels
 1001 exemplified with a staggered beam VIP. *Energy Build.* 42, 590–597.
 1002 <https://doi.org/10.1016/j.enbuild.2009.10.029>

1003 Kwon, J.S., Jang, C.H., Jung, H., Song, T.H., 2009. Effective thermal conductivity of various filling
 1004 materials for vacuum insulation panels. *Int. J. Heat Mass Transf.* 52, 5525–5532.
 1005 <https://doi.org/10.1016/j.ijheatmasstransfer.2009.06.029>

1006 Kwon, J.S., Jung, H., Yeo, I.S., Song, T.H., 2011. Outgassing characteristics of a polycarbonate core
 1007 material for vacuum insulation panels. *Vacuum* 85, 839–846.
 1008 <https://doi.org/10.1016/j.vacuum.2010.12.009>

1009 Lee, J., Song, T.-H., 2019. Conduction/radiation combined heat transfer with contact resistance for
 1010 application to vacuum insulation. *Int. J. Heat Mass Transf.* 129, 380–388.
 1011 <https://doi.org/https://doi.org/10.1016/j.ijheatmasstransfer.2018.09.085>

1012 Liang, Y., Wu, H., Huang, G., Yang, J., Wang, H., 2017. Thermal performance and service life of vacuum
 1013 insulation panels with aerogel composite cores. *Energy Build.* 154, 606–617.
 1014 <https://doi.org/10.1016/j.enbuild.2017.08.085>

1015 Lorenzati, A., Fantucci, S., Capozzoli, A., Perino, M., 2016. Experimental and numerical investigation of
 1016 thermal bridging effects of jointed Vacuum Insulation Panels. *Energy Build.* 111, 164–175.
 1017 <https://doi.org/10.1016/j.enbuild.2015.11.026>

1018 Ma, H., Zheng, X., Luo, X., Yi, Y., Yang, F., 2018. Simulation and analysis of mechanical properties of
 1019 silica aerogels: From rationalization to prediction. *Materials (Basel)*. 11, 1–12.
 1020 <https://doi.org/10.3390/ma11020214>

1021 Memon, S., Fang, Y., Eames, P.C., 2019a. The influence of low-temperature surface induction on
 1022 evacuation, pump-out hole sealing and thermal performance of composite edge-sealed vacuum
 1023 insulated glazing. *Renew. Energy* 135, 450–464.
 1024 <https://doi.org/https://doi.org/10.1016/j.renene.2018.12.025>

1025 Memon, S., Fang, Y., Eames, P.C., 2019b. The influence of low-temperature surface induction on
 1026 evacuation, pump-out hole sealing and thermal performance of composite edge-sealed vacuum
 1027 insulated glazing. *Renew. Energy* 135, 450–464. <https://doi.org/10.1016/j.renene.2018.12.025>

1028 Palyvos, J.A., 2008. A survey of wind convection coefficient correlations for building envelope energy
 1029 systems' modeling. *Appl. Therm. Eng.* 28, 801–808.

1030 <https://doi.org/10.1016/j.applthermaleng.2007.12.005>

1031 Paneri, A., Wong, I.L., Burek, S., 2019. Transparent insulation materials: An overview on past, present and
1032 future developments. *Sol. Energy* 184, 59–83.
1033 <https://doi.org/https://doi.org/10.1016/j.solener.2019.03.091>

1034 Spagnol, S., Lartigue, B., Trombe, A., Gibiat, V., 2007. Thermal modeling of two-dimensional periodic
1035 fractal patterns, an application to nanoporous media. *Europhys. Lett.* 78, 46005.
1036 <https://doi.org/10.1209/0295-5075/78/46005>

1037 Thiessen, S., Knabben, F.T., Melo, C., Gonçalves, J.M., 2018. A study on the effectiveness of applying
1038 vacuum insulation panels in domestic refrigerators. *Int. J. Refrig.* 96, 10–16.
1039 <https://doi.org/https://doi.org/10.1016/j.ijrefrig.2018.09.006>

1040 Woignier, T., Primera, J., Alaoui, A., Etienne, P., Despestis, F., Calas-Etienne, S., 2015. Mechanical
1041 Properties and Brittle Behavior of Silica Aerogels. *Gels* . <https://doi.org/10.3390/gels1020256>

1042 Yang, Z., Katsura, T., Aihara, M., Nakamura, M., Nagano, K., 2018. Investigation into window insulation
1043 retrofitting of existing buildings using thin and translucent frame-structure vacuum insulation panels.
1044 *Energies* 11. <https://doi.org/10.3390/en11020298>

1045 Yang, Z., Katsura, T., Aihara, M., Nakamura, M., Nagano, K., 2017. Development of numerical heat transfer
1046 and the structural model to design slim and translucent vacuum layer type insulation panels to
1047 retrofitting insulation in existing buildings. *Energies* 10. <https://doi.org/10.3390/en10122108>

1048